



Eidgenössische Technische Hochschule Zürich
Swiss Federal Institute of Technology Zurich

PAUL SCHERRER INSTITUT



BEAM CHARACTERIZATION OF LOW ENERGY ELECTRONS FROM A LASER WAKEFIELD ACCELERATOR

MASTER THESIS

Department of Physics
ETH Zurich

Author

BSc ETH PHYSICS
Nick Sauerwein

Supervisor

Dr. Andreas Adelman

Scientific Advisor

Dr. Rasmus Ischebeck

December 7, 2017



Declaration of originality

The signed declaration of originality is a component of every semester paper, Bachelor's thesis, Master's thesis and any other degree paper undertaken during the course of studies, including the respective electronic versions.

Lecturers may also require a declaration of originality for other written papers compiled for their courses.

I hereby confirm that I am the sole author of the written work here enclosed and that I have compiled it in my own words. Parts excepted are corrections of form and content by the supervisor.

Title of work (in block letters):

Beam Characterization of Low Energy Electrons from a Laser Wakefield Accelerator

Authored by (in block letters):

For papers written by groups the names of all authors are required.

Name(s):

Sauerwein

First name(s):

Nick

With my signature I confirm that

- I have committed none of the forms of plagiarism described in the '[Citation etiquette](#)' information sheet.
- I have documented all methods, data and processes truthfully.
- I have not manipulated any data.
- I have mentioned all persons who were significant facilitators of the work.

I am aware that the work may be screened electronically for plagiarism.

Place, date

Villigen, 07.12.2017

Signature(s)

For papers written by groups the names of all authors are required. Their signatures collectively guarantee the entire content of the written paper.

Abstract

The characteristics of low energy electrons accelerated by a laser wakefield are studied. A shock-front in the gas jet flow is used for particle injection. The work includes understanding the acceleration process, setting up the experiment and measuring properties like the charge, divergence and energy of the accelerated electrons. The experiment includes diagnostics for the laser, the electrons and the gas jet. In order to make high resolution energy distribution measurements with relative errors $\Delta E/E$ of below 10 %, a tunable electron spectrometer has been set up. A tunable permanent magnet quadrupole triplet allowed for setting of the stigmatic focus in a range from 5 keV to 5 MeV. For the experiment, a browser based interface (pyPECS) was developed. With a Faraday cup, electron acceleration to energies of the order of 60 keV was verified. With an acceleration length being 0.3 mm, an accelerating gradient above 200 MeV m^{-1} was achieved. The divergences of the accelerated bunches were of the order of 20 mrad.

Contents

Acknowledgments and Introduction to Project	V
1 Introduction	2
2 Principle of Laser Wakefield Acceleration	3
2.1 Plasma Wave Generation	3
2.2 Density Down-Ramp Injection	5
2.3 Acceleration Process	6
3 Experimental Setup for LWFA	8
3.1 Properties of the Laser	9
3.2 Properties and Design of the Plasma Source	10
3.3 Electron Diagnostics	13
3.4 The Electron Spectrometer	14
3.5 Timing of the Measurement	16
3.6 Control Software of Experiment pyPECS	18
4 Tunable Permanent Magnet Elements	21
4.1 Halbach Arrays	23
4.2 2D Analytic Expressions for Magnetic Field and Torque	24
4.3 Optimization of the Magnetic Field	28
4.4 Characterization of the Magnetic Field	29
4.5 Electron Equivalent of a Deformable Lens	32
5 Characterization of the Electron Bunches	33
5.1 Typical Features of Faraday Cup Signals	33
5.2 Dependence of FC Signals on the Accelerator's Configuration	35
5.3 Beam Size Measurements	37
6 Outlook	42
7 Appendix	44
7.1 Image Collection	44
7.2 Multipole Moments of Permanent Magnets	44
7.3 Field Maps of Permanent Magnet Lattice Elements	46
7.4 Collection of Python Scripts	49
7.4.1 Residue Calculation	49
7.4.2 Focus Optimization	49
7.4.3 Example Device (test_device1.py)	50
References	51

Acknowledgments and Introduction to Project

Before going into the technical details I want to express my gratitude towards all of the people that contributed to this project. This begins of course with Benedikt Hermann. Together, we took the initiative to build a particle accelerator during our studies. Naively, we contacted Günther Dissertori at ETH Zurich after a lecture on particle accelerators for the course "Introduction Particle and Nuclear Physics" and asked whether there was a possibility to build an accelerator as a student. He immediately contacted my supervisor Andreas Adelman. After a discussion about what accelerator to build, it became clear that we wanted to make a step forward and try to construct a laser wakefield accelerator. It is now the first in Switzerland.

We started by understanding the theoretical concepts of laser wakefield acceleration (LWFA) in a semester thesis [24]. In the thesis the linear model was extended and particle-in-cell simulations with the code WARP were made [30]. This was only possible because of the great support of Rémi Lehe from the Lawrence Berkeley National Laboratory.

In a semester thesis [12] and later in his master thesis [13] Benedikt Hermann developed the gas jet and a stable and fast method for its characterization [1]. The experimental work was made possible by help of my scientific advisor Rasmus Ischebeck and the expertise of many PSI employees.

In an internship at LLR at Ecole Polytechnique I learned a lot about the experimental implementation and theoretical description of electron spectrometers [25]. I thank my supervisor Arnd Specka for the fruitful and interesting discussions. They helped me with gaining knowledge about the electron spectrometers.

During my master's thesis I faced many experimental and design challenges. Regarding the solution of laser problems the members of the SwissFEL laser group (Christian Erny, Junpei Deng, Andreas Dax, Alexandre Trisorio and Christoph Hauri) showed great commitment. I want to thank them for giving us the opportunity to work with their Ti-Sa laser system.

In the design and experimental test of the tunable permanent magnet elements, the great support of the PSI Magnet Section (Stéphane Sanfilippo, Phillippe Lerch, Vjeran Vranković, Marco Negrazus, Roland Deckardt, and Roland Felder) and Insertion Devices (Thomas Schmidt, Marco Calvi, Marc Brügger, Steffen Danner and Marcus Schmidt) group was crucial. I want to thank Robin Sommer from Arnold Magnetics for the great support and the company visit.

At this point I want to thank Dominique Zehner for his great help. He made beautiful CAD drawings and helped a lot with the design and assembly of the permanent

magnet array and other parts of the experiment. I also want to thank Michael Eichenberger for the drawing of the deformable electron lens.

Without the excellent gold coating of the parabolic mirror, the focus of the laser wouldn't have been so good. I want to thank Michael Horisberger for the great help. I want to express my gratitude towards Cigdem Ozkan Loch, Daniel Treyer and Andreas Walker, who helped me understand and improve the signals.

I want to thank my girlfriend Nina Urfer for her great support. She sacrificed some days and evenings to help me with the experiments. Without her help I wouldn't have had the endurance to characterize the permanent magnets over the weekend until late in the night.

Finally, I want to thank my friends (Jeremy Stevens, Anna Mittelbach and Sven Wang) for taking the time to read my thesis.

1 Introduction

Particle accelerators are a frequently used tool to image small structures. They can be used for high energy physics to investigate the fundamental structure of elementary particles, or help us understand the structure and dynamics of matter which can be useful for biology, chemistry, medicine and physics. When accelerating to high energies these machines become large and expensive. Nowadays a lot of research is done to further increase the acceleration gradients (energy per acceleration length). In this respect, the field of laser wakefield acceleration (LWFA) seems very promising. Gradients that exceed the ones of conventional RF cavity acceleration structures by a factor of 1000 can be reached. In this thesis we study how LWFA can be used to accelerate electrons to MeV kinetic energies within a fraction of a mm. That this is possible has already been shown in some experiments [29, 26, 11].

The thesis has the following structure. First I give a short introduction to the key theoretical concepts of LWFA in the linear regime (see Section 2) which are essential to understand the experimental implementation (see Section 3). In order to characterize the kinetic energy of the accelerated electron bunches, a spectrometer is built. In Section 4 I give the arguments that lead to the permanent magnet design. Finally, the experiments conducted in order to characterize the accelerated electron bunches are discussed (see Section 5).

2 Principle of Laser Wakefield Acceleration

In this chapter we are going to discuss some important theoretical concepts used in the design and interpretation of the experimental setup presented in this thesis. They were derived in great detail in a semester thesis [24], but here we are rather going to focus on their physical implications and how they influenced the design of the experiment. The acceleration process of LWFA can be viewed as the “surfing” of electrons on a plasma wave. It is very helpful to keep the analogy of a wake surfer in mind. Wake surfing [35] is a sport where a person on a board (surfer) rides on the stern wave (wake) of a motor boat. During this process the energy of the motor boat is transferred to the surfer via the water. The driving/accelerating force of the surfer is the gravitational force down the slope of the wake. For LWFA this is very similar. Here a short laser pulse, with a duration of a few fs and a very high intensity (ranging from GW to PW), is focused onto a plasma. The plasma can be either pregenerated by capillary discharge or generated by the already very intense head of the laser, a process called self-ionization. The co-propagating wave (wake) generated by the laser (boat) in the plasma (lake) contains strong electro-magnetic forces (gravitational force) that can accelerate so called “injected electrons” (surfer) to high kinetic energies. In the following Sections, three fundamental questions will be answered: how the plasma wave is generated (Section 2.1), how the electrons are injected into the waves (Section 2.2) and finally how they are accelerated to high kinetic energies (Section 2.3).



Figure 1: Image of a professional wake surfer [5].

2.1 Plasma Wave Generation

The core of LWFA is the generation of a wave in a plasma by a laser pulse. It turns out that the shape of the wake depends strongly on the normalized intensity of the laser pulse $a = \frac{eA}{mc}$, which is unitless¹. When $a \ll 1$, so at relatively low intensities, one speaks of the linear regime². In the case of a homogeneous plasma an analytic expression for the wake can be derived using Maxwell’s and Euler’s equations and by assuming an ideal shape for the pulse (Gaussian or \cos^2) [9]. The main result is that close (one plasma wavelength

¹In all the theoretical derivations with respect to plasma wakes, the cgs units convention was applied. Often normalized quantities are introduced to better understand the scaling.

²Linear comes from the fact that in this regime the approximation of truncating the equations after the first order is valid ($a^2 \approx 0$). In the case of the non-linear regime ($a > 1$) the wake shape can also be approximated [9]. For this master thesis it is not of high interest because the energy of the laser pulses is too low to reach this regime.

λ_p) behind the laser pulse the generated wave has a harmonic shape

$$\Phi = \Phi_0 \frac{\pi}{4} \exp\left(-\frac{r^2}{r_0^2}\right) \sin\left(\frac{2\pi}{\lambda_p} \xi\right),$$

where $\Phi_0 = \frac{mc}{e} = 1.6 \times 10^8$ V(SI units) is a constant, $\xi = (z - v_g t)$ is the co-moving coordinate of the laser and v_g is the group velocity of the laser that depends on the density of the plasma. The $\frac{\pi}{4}$ is a geometrical factor. It is different depending on the shape of the laser and the resonance of the wake. To get $\frac{\pi}{4}$ one has to assume a \cos^2 longitudinal intensity profile, and the plasma wavelength $\lambda_p = 2L$ must be matched to twice the full width at half maximum (FWHM) length L of the laser pulse. This is not precisely the resonant condition ($\lambda_p \approx 2.5L$) [17], but it is easier to calculate analytically.

The derivation of this result relies on the following simple picture. As the laser pulse propagates through the plasma, the electrons feel the electric and magnetic fields of the laser. The field forces the electrons to follow a wiggled motion, called the quiver motion (see Figure 2). These fast oscillations lead to an increase in the mean kinetic energy of the electrons ($E_{kin}(v^2)$). When averaging the equations of motion over the time of one oscillation period $T = \nu^{-1}$, where ν is the laser's carrier frequency, the increase in kinetic energy turns into an increase of potential energy for the slower drifting motion of the electron. This effective potential energy is called the ponderomotive potential $\Phi_p = mc^2 \bar{\gamma} \approx eA$, where $\bar{\gamma}$ is the mean of the relativistic γ factor of the electrons at a specific position in the plasma. So the potential is high where the laser intensity is high. This means that the electrons are pushed out of this region. The heavy ions, however, are less affected because of their weight. As the electrons are deflected out of the region

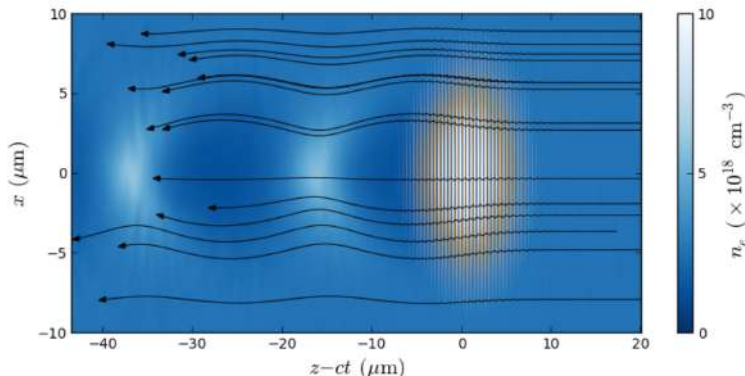


Figure 2: Illustration of the plasma wave in the reference frame of the laser $\xi = z - ct$ ($v_g \approx c$). The laser (orange) is propagating to the right. The black lines show the trajectories of the electrons in the plasma [17].

of the laser, there will be less of them behind the laser. This leads to a positively charged region. Because of the Coulomb force, the electrons are attracted by this region and then form a negatively charged region right behind the positive one. They are then repelled again by the negative charges. This argument repeats for several cycles until the energy of the oscillation is lost by radiation and collisions. In equation 2.1 the analytic form of the electrostatic potential is shown.

2.2 Density Down-Ramp Injection

So far we have discussed how the plasma wake is generated in a homogeneous plasma. We have seen that strong electric fields up to $\Phi_0/\lambda_p \approx 1 \times 10^{15} \text{ V m}^{-1}$ are generated that could potentially accelerate electrons to high kinetic energy in short distance. However, so far the electrons just follow an oscillatory path (see Figure 2) of the order of the plasma wavelength (here $\sim 10 \mu\text{m}$). A process that injects some electrons into the right phase of the wave such that they feel an accelerating force over a large distance (here $\sim 1 \text{ mm}$) has to be implemented. A simple method is density down-ramp injection. Here injection is achieved at the abrupt transition between high and low density plasmas. Indeed, to achieve the best possible acceleration, the electron density of the low density plasma is chosen so that the plasma wavelength $\lambda_p = \sqrt{(\pi c^2 m)/(n_e e^2)}$ and pulse length $c\tau$ are similar ($\lambda_p \approx 2.5L$), thus entering into resonance ($n_e = n_{opt}$).

Before explaining how a sudden change in density can trigger injection, we first have to develop an understanding of the term separatrix. Injecting an electron into a wave means that the movement of the electron is no longer oscillatory, but rather the electron follows the wave. Intuitively, this means that the velocity of the particle has to exceed that of the wave v_g at some point. In a 1D model which assumes that $r = 0$ for the accelerated particles, one can calculate the trajectory in phase space of the particle whose velocity at the end of the accelerating phase of the wave exactly matches the speed of the wave. This means that the electron will not enter the decelerating phase. It will propagate through the accelerating phase again, but now in the opposite direction with respect to the co-moving coordinate ξ (similar to the black trajectory in Figure 5). This trajectory is called 1D separatrix. All trajectories lying above this trajectory in phase space will contain velocities that exceed that of the plasma wave, which means that these particles are accelerated to high energies and therefore they are injected. Figure 3 shows the trajectories of electrons that form the wake (solid blue line) in high density ($n_e = 2n_{opt}$) plasmas. It intersects with the separatrix at the resonant density (dashed green line). So if the density changes from high (non-resonant, short wave length) to low (resonant, long wave length), some wake electrons are suddenly in the right phase to be injected. The model used to describe the process makes the assumption that the transition between the two different densities is sudden, so smaller than the plasma wave length.

At this point it is important to note that the laser parameters set in Figure 3 are very optimistic. In fact the focal spot size r_0 and pulse length τ are larger (see Table 1). Nevertheless, a density down-ramp can have an impact on the energy of the accelerated electrons. Even if the normalized intensity a_0 is too low to accelerate electrons to the group velocity v_g of the laser in half the plasma wavelength, the density down-ramp has the effect of increasing the momentum amplitude of the oscillatory movement of the electron in the plasma wake (see Figure 4).

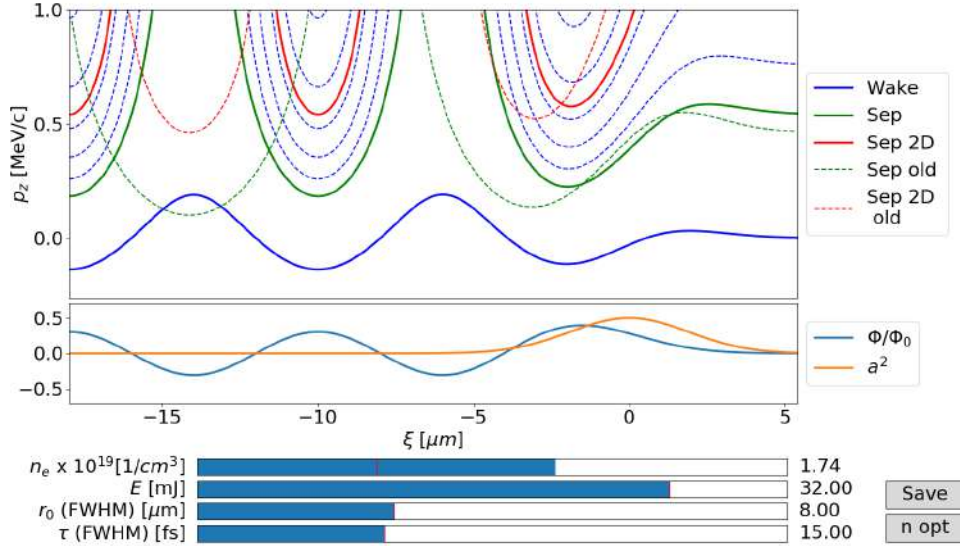


Figure 3: Screenshot of the python program that models DDR injection. The program had been written during my semester thesis [24]. Sep stands for 1D separatrix and Sep 2D for the 2D separatrix. The dashed green and red lines show the 1D and 2D separatrix in the case of resonant density ($n_e = n_{opt}$). The electrons forming the wake before the density down-ramp ($n_e = 2n_{opt}$) follow the solid blue trajectory.

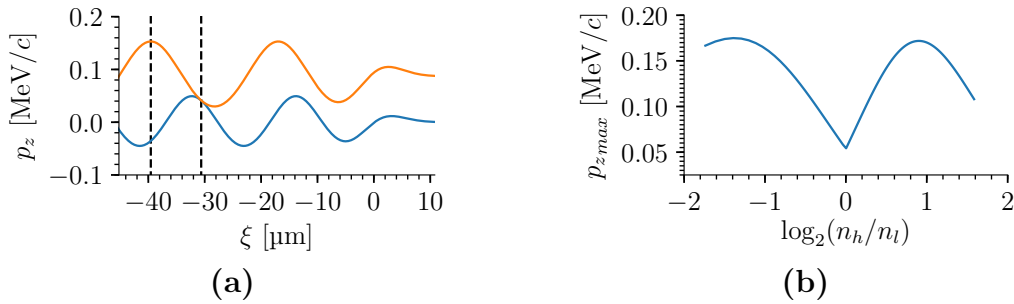


Figure 4: Effect of the density down-ramp on the energy of the accelerated electrons. In Figure 4a the solid blue line shows the trajectory of the electrons that form the wave ($n_e = 2n_{opt}$). The orange trajectory (for low plasma densities, $n_e = n_{opt}$) is the one that intersects with the blue, but has maximal momentum p_z . So if the density changes rapidly, electrons from the wake in the high density plasma which followed the blue line, suddenly follow the orange line. This leads to a higher maximal momentum. Figure 4b shows how the maximal longitudinal momentum varies as a function of the ratio between the high (n_h) and low (n_l) electron density. Here the laser parameters are chosen as in Table 1.

2.3 Acceleration Process

In this Section we are going to give a qualitative picture of how the electrons are accelerated. Depending on the phase of the particles in the wake, the force is accelerating ($\xi \in [-\frac{3}{2} - \lambda_p, -2\lambda_p)$), decelerating ($\xi \in [-2\lambda_p, -\frac{5}{2}\lambda_p)$), focusing ($\xi \in [-\frac{7}{4}\lambda_p, -\frac{5}{4}\lambda_p)$) or defocusing ($\xi \in [-\frac{9}{4}\lambda_p, -\frac{7}{4}\lambda_p)$). In an optimal wakefield accelerator, the electrons should be simultaneously in the accelerating and focusing regions during the entire acceleration

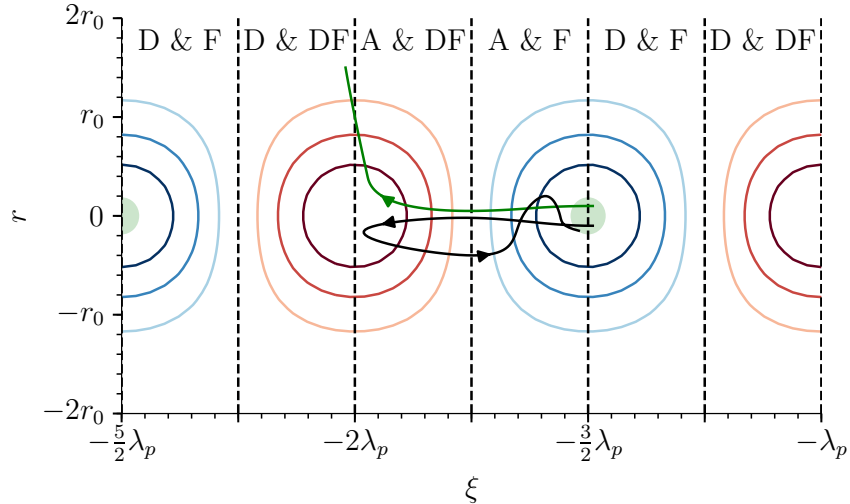


Figure 5: Qualitative sketch of typical trajectories of accelerated electrons in a plasma wake. The contours correspond to $-\Phi$ (equation 2.1). These trajectories have not been calculated. The electrons are injected in the green region. They are either deflected (green) or become trapped in the wake (black). The different regions of dynamics are divided by the dashed black lines. These regions are decelerating (D), accelerating (A), transversally focusing (F) or defocusing (DF).

process. The trajectory of the particle with minimal energy that fulfills this condition in the 1D model is called 2D separatrix (see Figure 3). In case of a laser in the linear regime ($a < 1$) and density down-ramp injection however, the force on the electrons is not high enough to accelerate them within the accelerating and focusing region to the group velocity v_g of the laser. They therefore enter the accelerating and defocussing region. Here there are three qualitatively different cases. If the wake is strong enough, the electrons' velocity will exceed the group velocity v_g of the laser and the electrons reenter the accelerating and focusing region (black line in Figure 5). These electrons will have small divergences and very high energies (\sim MeV). For this to happen the longitudinal phase-space coordinates must, by definition, lie above the 1D separatrix (see Figure 3). This case only occurs if the electron had an initial position close to the laser propagation axis ($r = 0$) and the wakefield is strong enough. Otherwise, if the energy of the laser is too low or the initial radial position of the electron is too large, it will either drop into the next valley of the potential landscape or be deflected by the strong defocusing fields (green line in Figure 5). Following the argument presented at the end of Section 2.2 (see Figure 4), the kinetic energies of such electrons can be up to 100 keV. Taking the parameters of the experiment into account, it is very plausible that we are observing the last of these cases in our experiments. In Section 5 the results that support this hypothesis are presented.

3 Experimental Setup for LWFA

In Figure 6 the whole experimental setup that is related to LWFA is illustrated. In the Appendix 7.1 images are shown so that the dimensions are clear. The Ti-Sa laser pulse (light yellow) is focused with a 90° off-axis parabolic mirror³ onto Argon gas (light blue) in a vacuum (light gray) chamber. In order to aim the laser onto the gas jet, the parabolic mirror is mounted on a 3D periscope which enables scans in the range of ± 25 mm in all three dimensions. The position of the laser focus with respect to the gas jet nozzle can be determined by two cameras from the bottom and from the side. Using a small pixel size camera we can optimize the focal spot size of the Ti-Sa laser by changing the pitch and roll of the motorized parabolic mirror. The supersonic gas flow (blue) out of the jet (dark gray) is perturbed by a blade (black) which can be moved in the stream (rotation and in/out). At the edge of the knife a shock front is created which leads to a double plateau density distribution needed for density down-ramp injection. It can be measured with a single-beam Wollaston interferometer setup that makes use of a He-Ne laser (red) [1]. Through the process of LWFA (see Section 2) electrons (green) are accelerated in the propagation direction of the Ti-Sa laser. The electron bunches are analyzed using either a Faraday cup, a screen or a spectrometer. However, for this thesis only measurements with the Faraday cup were performed. The spectrometer consists of tunable permanent magnets that make up a quadrupole triplet (dark blue) and a dipole (dark yellow). In the following Subsections more details about the specific features of the experiment are presented. Finally, the software that was developed to control all the devices is discussed (see Section 3.6).

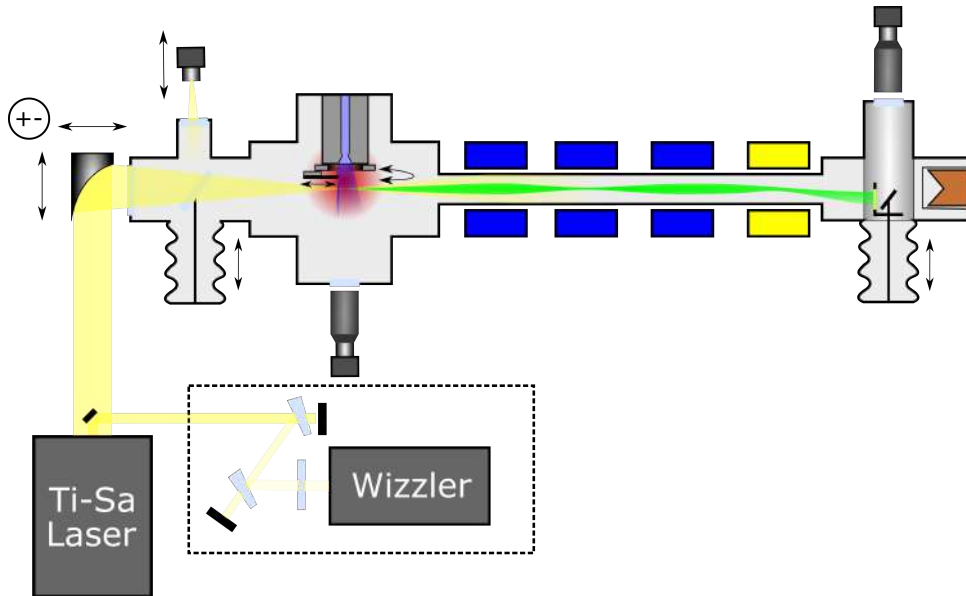


Figure 6: *Sketch of LWFA experiment at PSI.*

³The mirror was coated with a (100 ± 5) nm gold layer. The thickness of the gold layer was measured with a profilometer.

3.1 Properties of the Laser

The laser is the driving element of the acceleration. It is therefore important to understand its properties, like its temporal profile, peak intensity, focal spot size and positioning fluctuations in great detail. In the experiment we have three devices that give us the possibility to probe these properties. First there is the energy-meter to measure the energy contained in a single pulse. Second the WIZZLER, a device that can measure the temporal pulse profile. Last we have a camera that can observe the focal spot size directly.

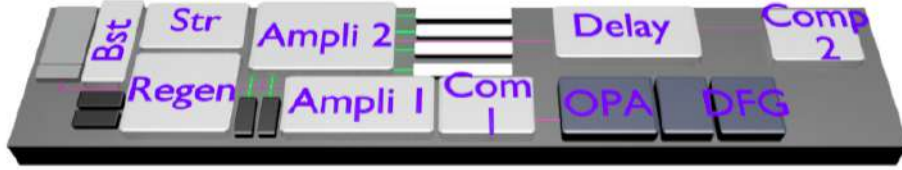


Figure 7: Sketch of the laser setup used for the experiment [16]. The beam before the OPA was taken for our experiments.

Temporal Profile The WIZZLER is a device produced by Fastlite [20, 31]. It makes use of a process called “self-referenced spectral interferometry” (SRSI). The process is based on the fact that if two pulses with similar intensities are separated by a time τ and the temporal profile of one of the pulses is dependent on the other, the fringes in the resulting spectrum give informations about the spectrum as well as the phase of the pulse. Therefore, the complete temporal profile can be reconstructed using a Fourier transform. Figure 8 shows a schematic drawing of how such pulse replicas are generated.

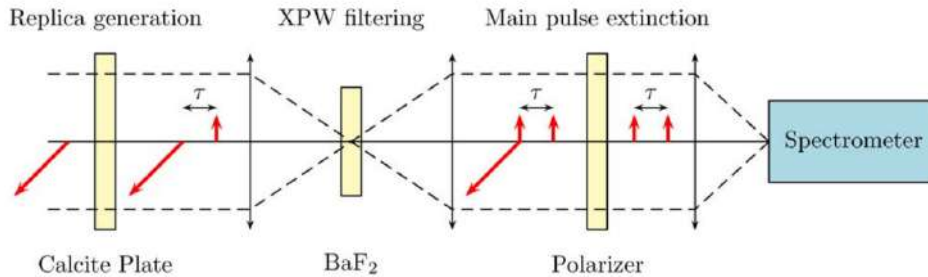


Figure 8: Replica generation in WIZZLER [20].

If one takes a birefringent plate, where the slower nominal axis (with higher refractive index n_s) is rotated by a small angle with respect to the laser pulse polarization, two pulses that are distanced by $\tau = L (n_s - n_f)/c$ are generated. These two pulses have different energies and of course polarization (tilted by 90°). In order to see the fringes in the spectrometer these two pulses have to interfere, which means that they need to have the same polarization. A pulse energy sensitive method of rotating the polarization by 90° is the non-linear effect “cross-polarized wave generation” (XPW). The process

will generate a 90°-rotated pulse component. Since the process is non-linear (specifically: 3rd order) only the pulse with higher intensity (second pulse) will generate a rotated component. After filtering out the remaining high intensity component of the second pulse with a polarizer, the desired configuration is created, which then allows for a pulse length measurement. The laser system also makes use of the DAZZLER[14], which can change the phase and amplitude of different frequencies using an acousto-optical effect. Together with the WIZZLER we were able to optimize the pulse length to about 30 fs.

Focal Spot Size and Positioning Fluctuations The position and size of the focal spot of the laser was monitored using a camera (Basler acA 3800-10gm) with a pixel size of 1.67 μm . Since the mirror mount of the parabolic mirror was motorized we were able to optimize the focal spot shape and size in a feedback loop. The optimization was a minimization of the sum of squares of the Full Width at Half-Maxima (FWHM) and the eccentricity, i.e. $f = \text{FWHM}_x^2 + \text{FWHM}_y^2 + (\text{FWHM}_x - \text{FWHM}_y)^2$. Numerically the minimization was realized with the numpy implementation of the Nelder-Mead method [34], which has the advantage that the initial step doesn't have to be specified and it doesn't forget good configurations like a regular gradient descent algorithm. The full width at half maximum was extracted from the images by finding the half maximum contour using the `find_contours` algorithm in the `scikit-image` package [32]. See Section 7.4.2 in the appendix for the implementation. After the optimization was finished we could check the focus with the focus camera (see Figure 9). It showed that we could reach a spot size (FWHM) of 11 μm , which was the termination condition of the minimization. In fact, this size is far from ideal. For a perfect Gaussian shape a spot size of 7.2 μm is expected. The difference between the two values might be due to a distorted wavefront, but so far no measurement has been made to check this. The expected Rayleigh length for a 11 μm spot size is 0.34 μm .

Laser Pulse Energy (AL)	(36 ± 1) mJ
Transmission of Laser Line*	0.88 ± 0.02
Laser Pulse Energy (IP)*	(32 ± 1) mJ
Laser Pulse Length (FWHM, IP)	(30 ± 2) fs
Focal Spot Size (FWHM, IP)	11 μm
Rayleigh Length (IP)*	0.34 mm

Table 1: Summary of laser parameters. The data is taken either at the iteration point with the plasma (IP) or right after the compressor (AL). The asterisk (*) denotes values calculated from other measurements.

3.2 Properties and Design of the Plasma Source

The key for LWFA is the plasma source, the design of which is very dependent on the properties of the laser. According to previous studies, it only makes sense to use pre-generated plasma sources when suitably tailored plasma densities for laser guiding are needed [27]. However the complexity is such that it exceeds the scope of this thesis. The simplest is to use a non-ionized Argon gas jet and rely on the propagation of a laser in a self-generated plasma [24]. In the case of a low pulse energy laser (36 mJ) and density

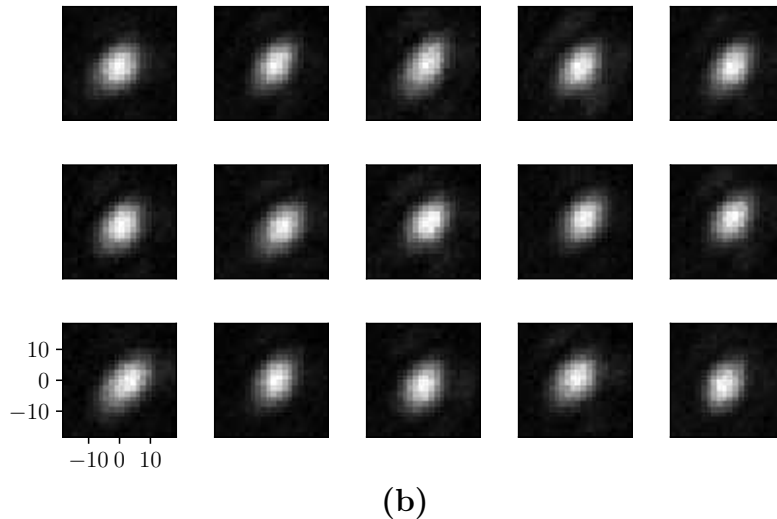
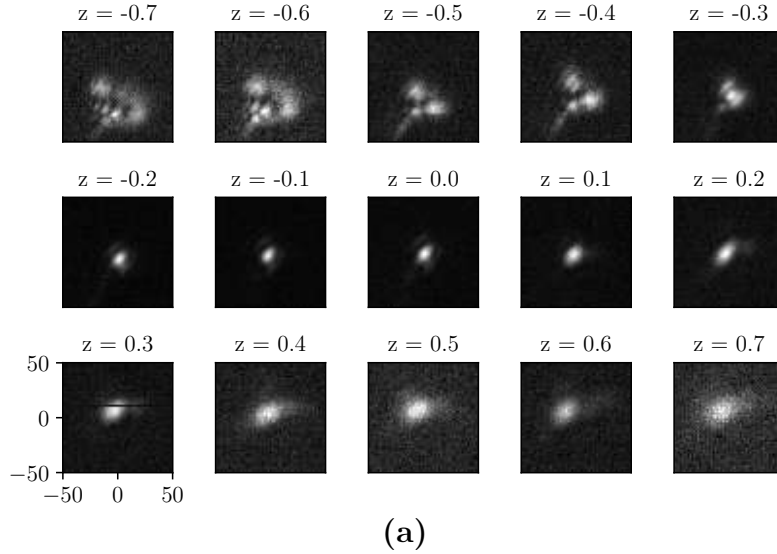


Figure 9: *Focal spot size and positioning fluctuations after the optimization. Image (a) shows a scan of the focus in the longitudinal direction and image (b) fifteen consecutive measurements of the focal spot.*

down-ramp injection, high laser intensities are needed. Therefore the laser has to be focused to a small focal spot of $11\ \mu\text{m}$. The resulting Rayleigh length is of the order of $0.34\ \text{mm}$. This limits the length of the acceleration and consequently the diameter of the gas jet at the level of its interaction with the laser to a fraction of a millimeter. The density at this height has to be chosen such that the plasma wake is generated most efficiently (see Section 2.1). The last condition is that the density profile should have a density down-ramp for injection (see Section 2.2) which should be as short as possible [8]. Most of the design arguments are nicely discussed in Benedikt Hermann's master thesis [13]. In this Section we will summarize his arguments and discuss the modifications that were made in order to get the electron beam described in Section 5.

Taking all necessary conditions for electron injection and acceleration into account, we came up with the idea of using a Parker solenoid valve with a conical outlet (Parker 009–0442–900). In our configuration, it can handle backing pressures up to 5 MPa and therefore densities up to several 1×10^{19} Argon atoms/cm³. A razor blade was fixed on a linear stage above the outlet of the gas jet. The blade generates a shock front in the supersonic gas flow (similar to a fighter jet in air). In the shockwave the gas densities can be up to two times higher than in the undisturbed gas flow [13]. In the first version of the blade setup which was used in Hermann’s master thesis, the distance between the blade and the nozzle output was 1 mm. At this relatively large distance from the nozzle the diameter of the gas distribution is already of the order of a millimeter (FWHM). Furthermore the size of the blade mount didn’t allow the laser focus to get closer than 2.6 mm from the nozzle. This meant that the diameter of the jet and therefore the acceleration length had to be of the order of several millimeters which is too long for the best configuration. We therefore modified the setup so that the distance between the blade and the nozzle was reduced to 50 μ m. Consequently, the size of the blade’s fixation was such that the focus of the laser could be as close as 0.5 mm from the blade.

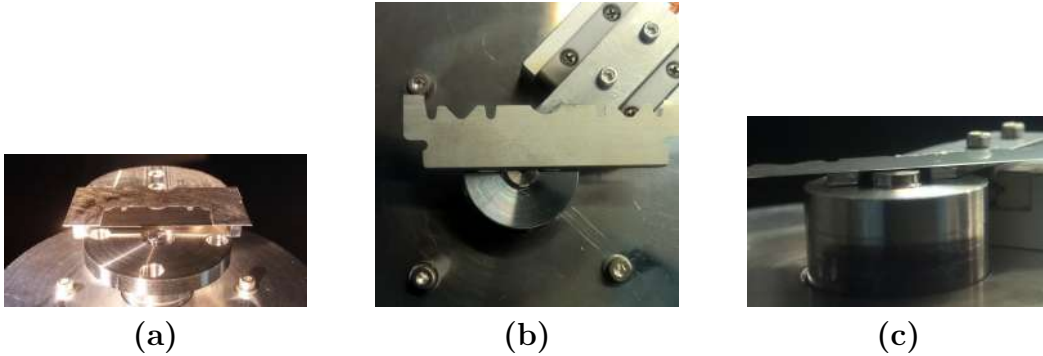


Figure 10: *Images of the gas jet nozzle. In (a) shows the nozzle and blade combination as it was used in Hermann’s thesis [13]. Figures (b) and (c) show the setup used to get the results presented in this thesis.*

The blade is mounted on top of a combination of a linear and a rotational stage. The linear stage is necessary because we want to be able to sweep over the positions of the blade with respect to the jet axis to find the optimal injection condition. The rotational stage however was used for the characterization of the gas density distribution. The rotation allows us to take interferometric projections from different angles, from which the 3D density distribution can be reconstructed by means of tomography. During my thesis we included the interferometer in the pyPECS control system (see Section 3.6) and sped up the computation by making use of graphics processing units (GPU). This allows for real-time reconstruction of the density distribution [1] and helped with finding the optimal conditions for a LWFA plasma source.

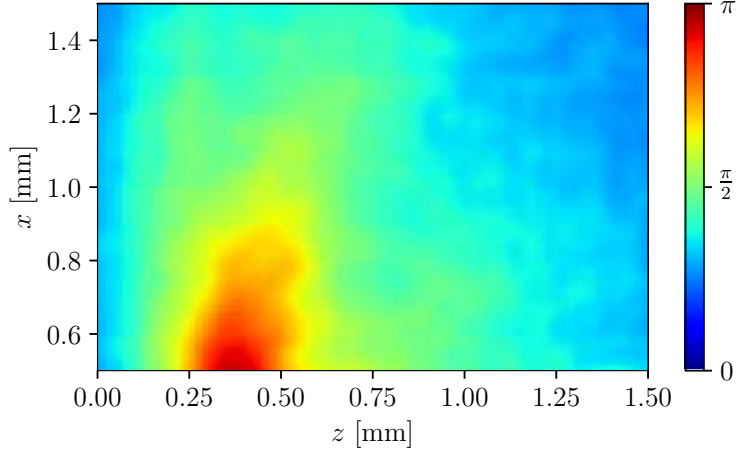


Figure 11: *Phase advance of the He-Ne laser in the gas distribution in the setup with the updated blade fixation. The shock front is visible in red. Here x is the vertical distance from the blade and z is measured parallel to the laser axis.*

3.3 Electron Diagnostics

In order to measure the charge, the divergence and the energy distribution of the particle beam, electron diagnostics are needed.

Faraday Cup For the first experiments, where low charges and huge divergences ($\gg 10$ mrad) are expected, a very sensitive large surface Faraday cup (FC) was developed [13]. This cup can measure charges down to a few fC spread out on a circular surface of 9.4 mm^2 . To avoid measuring disturbances from the laser⁴ or radio frequency waves, the front of the FC was shielded by a grounded aluminum foil. The way the foil was pressed on the cup had a huge influence on the signal. This will be discussed in Section 5 where the properties of the observed signals are discussed. The electrical signal of the cup is amplified and then digitalized by an oscilloscope (LECROY WS44MXs–B 400 MHz). As an amplifier we used the ZKL–1R5+ from mini-circuits with a bandwidth of 10–1500 MHz, a power amplification of 40 dB and termination of 50Ω which results in voltage amplification by a factor 100. As discussed in Section 3.5, the oscilloscope is triggered by a photo diode to avoid large signal jitter. Because of its huge acceptance area the FC can only be used to measure the charge of the electron bunch, but not how it is distributed in space. The trick is to clip the beam with a movable beam block (see Figure 12c) and reconstruct the distribution as a function of block position. This method allows for a measurement of the charge distribution of electrons along one spatial direction even if the charge flux is very low (see Section 5.3). A great disadvantage of the cup is that, if not properly shielded, it is sensitive to radio frequency excitations in the chamber. This can lead to wrong interpretations of the measured signals.

⁴If the cup is mounted close to the laser’s focal spot, the intensity of the laser is so high that electrons can be ripped out of the cup. This results in a positive charge on the FC.

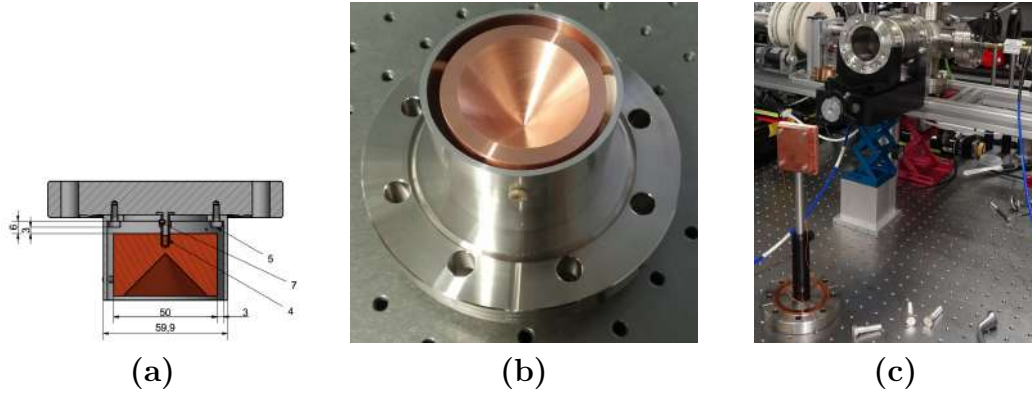


Figure 12: CAD drawing and image of the Faraday cup and the beam block. When the FC was installed in the vacuum chamber, the front was covered with aluminum foil. Image (c) shows the copper block and the linear vacuum stage that were used to clip the electron beam (see Section 5.3).

Scintillating Screen A scintillating screen that is shielded against laser light by aluminum foil can be used to measure both the charge and its distribution in space simultaneously in a single-shot. Since the screen is only sensitive to ionizing radiation, like UV, X-rays and electrons, the measured distributions cannot be generated by low frequency radiation that is generated in the plasma (Visible Light, IR, THz and RF). The drawback of the scintillator is its sensitivity. For our experiments both Yttrium aluminium garnet (YAG) crystals and a Kodak Lanex fast screen were used. However, no correlated signals could be observed.

Scintillating Fiber Another very sensitive method of detecting ionizing radiation or charged particles like electrons is a scintillating fiber. Like a scintillating screen, this method relies on optical excitations of a scintillating material and is therefore resistant to long wavelength electro-magnetic pulses. The fiber is coupled to a photo multiplier tube which allows for single photon counting. The issue with the fiber is that it cannot measure the distribution of the deposited charge, nor can it cover a large area.

3.4 The Electron Spectrometer

Based on simulations [24] the expected electron beam has a divergence of at least 10 mrad. In order to reach a good relative energy resolution $\Delta E/E$ of at least 10% the deflection angle of a single dipole magnet would have to be higher than 0.1 rad [25]. This corresponds to a beam cross-section on the order of tens of cm on the screen at a distance of half a meter. The charge of the beam however will be in the pC range. In combination with a large divergence, this means that the energy distribution cannot be extracted with a simple scintillating screen and therefore single shot distribution measurements become impossible. In order to solve this problem, focusing magnets were installed before the dipole. The unit consists of three tunable permanent magnet quadrupoles (see Section 4), which are tuned for stigmatic focus of a specific energy E_0 on the scintillating screen. This reduces the size of the beam on the screen and therefore increases the intensity of the scintillation light generated. The tunability of the quadrupole magnets allows to set

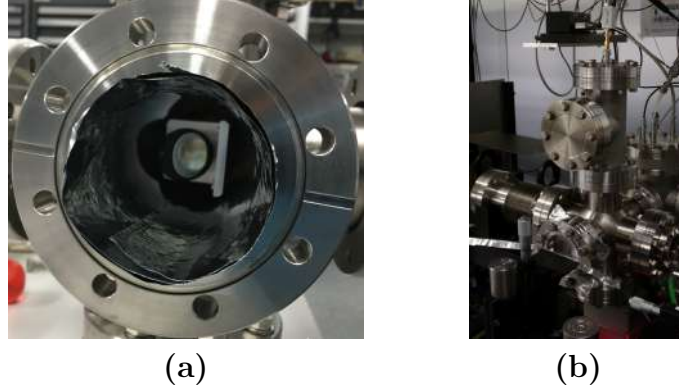


Figure 13: Images of the scintillating diagnostic tools. In Figure 13a an image of the screen setup is shown. A mirror that is mounted at 45° to the electrons' propagation direction allows the observation of the screen from the side (see Figure 6). Figure 13b shows the electron diagnostics chamber with the FC mounted on top (pickup mode). The scintillating fiber (bottom left) is used to detect ionizing radiation that passes through the aluminum foil.

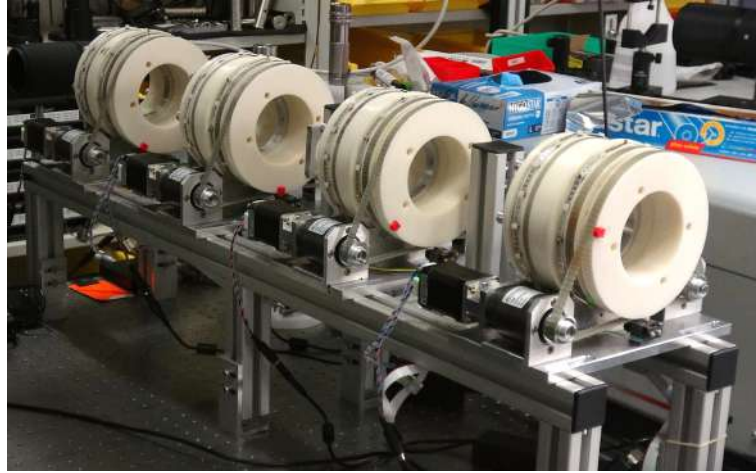


Figure 14: Setup of the permanent magnet spectrometer. Here just the beam pipe was missing and the magnets were not yet mechanically aligned. The first three magnets from the right are the quadrupoles $Q1$, $Q2$ and $Q3$. The last magnet on the left is the dispersing dipole magnet $D1$.

E_0 between 5 keV and 5 MeV. The strength of the dipole can also be adjusted so that for different energies E_0 the position of the focal spot is the same. All the calculations done for the design of the spectrometer are based on the theory developed in an internship at Laboratoire Leprince-Ringuet (in2p3) at Ecole Polytechnique supervised by Arnd Specka [25]. The results can be summarized as follows. Similar to optical lenses, a quadrupole triplet shows chromatic behavior. This means that for high ($E > E_0$) and low ($E < E_0$) energies the focal spot⁵ lies either behind or in front of the screen respectively. For E_0 however, the position of the electron on the screen doesn't depend on the initial angle of divergence x' . Thus it only depends on the position and size of the electron source

⁵Because the chromatic behavior is different in the two transverse directions, one cannot really speak of a focal spot anymore. It becomes astigmatic.

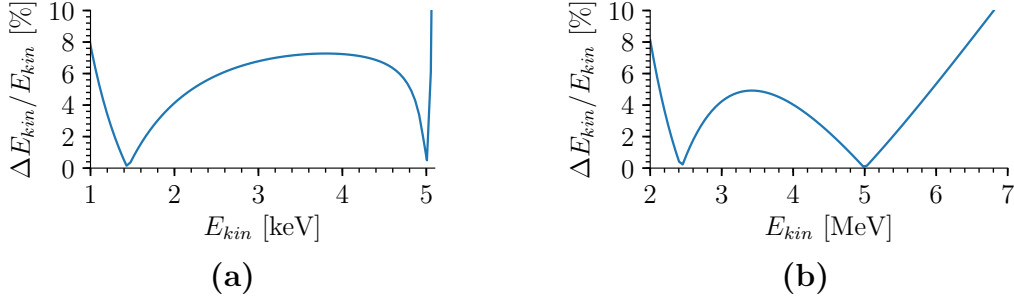


Figure 15: Resolution of spectrometer for two different stigmatic focus conditions, $E_{kin0} = 5 \text{ keV}$ (Figure 15a) and $E_{kin0} = 5 \text{ MeV}$ (Figure 15b).

(which is negligible in case of LWFA) and the energy of the particle. Hence, an enhanced resolution around the energy E_0 is achieved. Such a spectrometer also allows for single-shot emittance measurements [4, 33]. When using a quadrupole triplet in can happen that one of the two transverse directions (x or y) shows achromatic behavior⁶. This means that for two different energies E_0 and E_1 the beam is focused in this direction. When choosing the double-focused direction for dispersion by the dipole, two resolution optima of the spectrometer can be achieved (see Figure 15). This allows for broad range and high resolution measurements even if the divergence and energy spread of the beam is high.

3.5 Timing of the Measurement

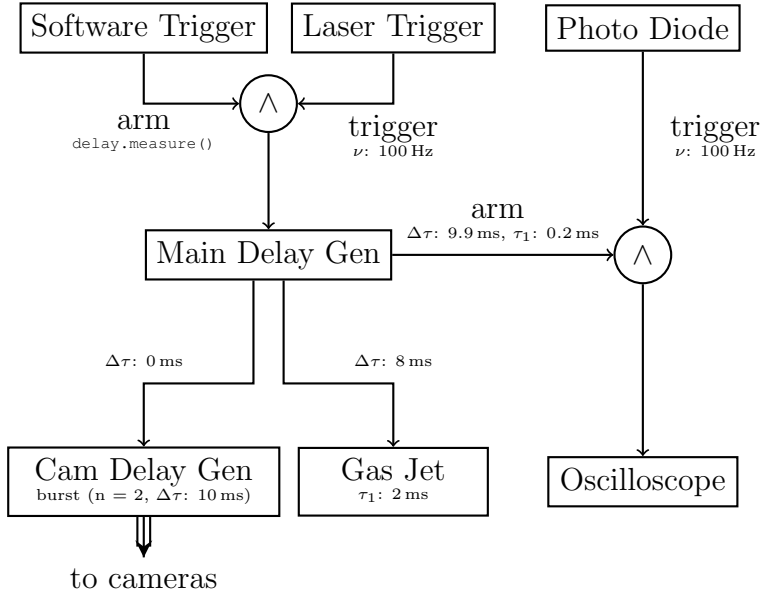


Figure 16: Schematic drawing of the trigger logic.

⁶To get two stigmatic focuses for two different energies E_0 and E_1 , at least 4 quadrupole magnets are needed. This configuration of quadrupoles is known as the “Russian quadruplet” [21].

The laser pulse, the gas jet opening and closing, the cameras' exposures and the oscilloscope must be synchronized. For all experiments, the laser was shooting continuously with a frequency of 100 Hz. The gas jet however should only open when the experimentalist (or the computer control system) wants to make a measurement. The jet needs to be opened before a laser pulse arrives. It takes about 2 ms until the valve of the jet is completely opened. So when the experimentalist gives the order to shoot (`delay.measure()`), the main delay generator (SRS DG645) gets armed to trigger at the next rising edge in the laser trigger signal. This signal is also used by the laser system to generate the laser pulse. The main delay generator triggers the devices, such that a measurement at the next arriving laser pulse can be made. Explicitly, it starts the opening process of the gas jet 8 ms after the first laser pulse arrived, triggers the camera delay generator and arms the oscilloscope that is then triggered precisely (jitter < 1 ns) with a photo diode. The camera delay generator is setup so that the cameras will always take two pictures (1. gas & laser, 2. only laser). The second picture is used for background subtraction.

3.6 Control Software of Experiment pyPECS

When we started with the LWFA experiments, the setup was still quite simple. Just the laser periscope had to be controlled from the computer. The only device to save live data from was the oscilloscope (Faraday cup). This was done by saving the waveforms as `txt`-files directly on the hard drive. With the use of a lab notebook the different configurations of the experiment were referenced to the data. But as soon as we began correlating results to the blade position, the backing pressure of the gas nozzle, the density profile, the intensity of the laser or the position of the linear stage in the compressor, documentation became very complicated. We therefore decided to code a universal experiment control software called pyPECS (python Physics Experiment Control Server), that is capable of taking care of documentation and live visualization of the results in a single unified interface.

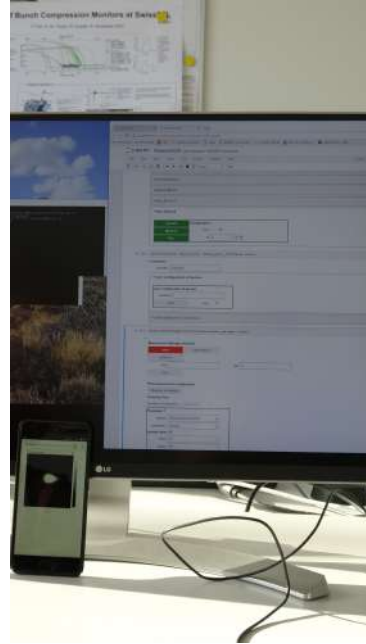


Figure 17: Usage example of pyPECS. Here a desktop computer is used to change the configurations of the devices or make measurements. The plots can be shown on both the computer and the smartphone.

The program was written in Python because of its object-oriented structure, numerical capabilities and large programmer community. On the Internet, a lot of packages can be found that allow communication with devices over Ethernet, USB or Serial. As an interface to interact with the control software we decided to use Jupyter notebooks [15]. Jupyter is a browser-based python editor which allows writing notebooks. The notebooks have a very similar structure to Mathematica notebooks. Because the editor runs in the browser, it can be accessed by all devices that can open web pages. So we can use laptops, desktops, tablets and even smartphones to interact with the experiment and show the results on all of them at the same time.

The diagram in Figure 18 illustrates the fundamental structure of the software. In principle there are three major classes, each dealing with specific tasks related to controlling an experiment. The device pool handles the communication with the devices. Its purpose is to build up the connection to the devices and read or change their configurations. In the device pool class, the devices which should be measured or plotted are specified. However, the actual measurement is handled by the measurement manager. It handles simple measurements, parameter sweeps or parameter optimizations by launching dedicated python threads that call the `measure` function for each device objects that have the attribute

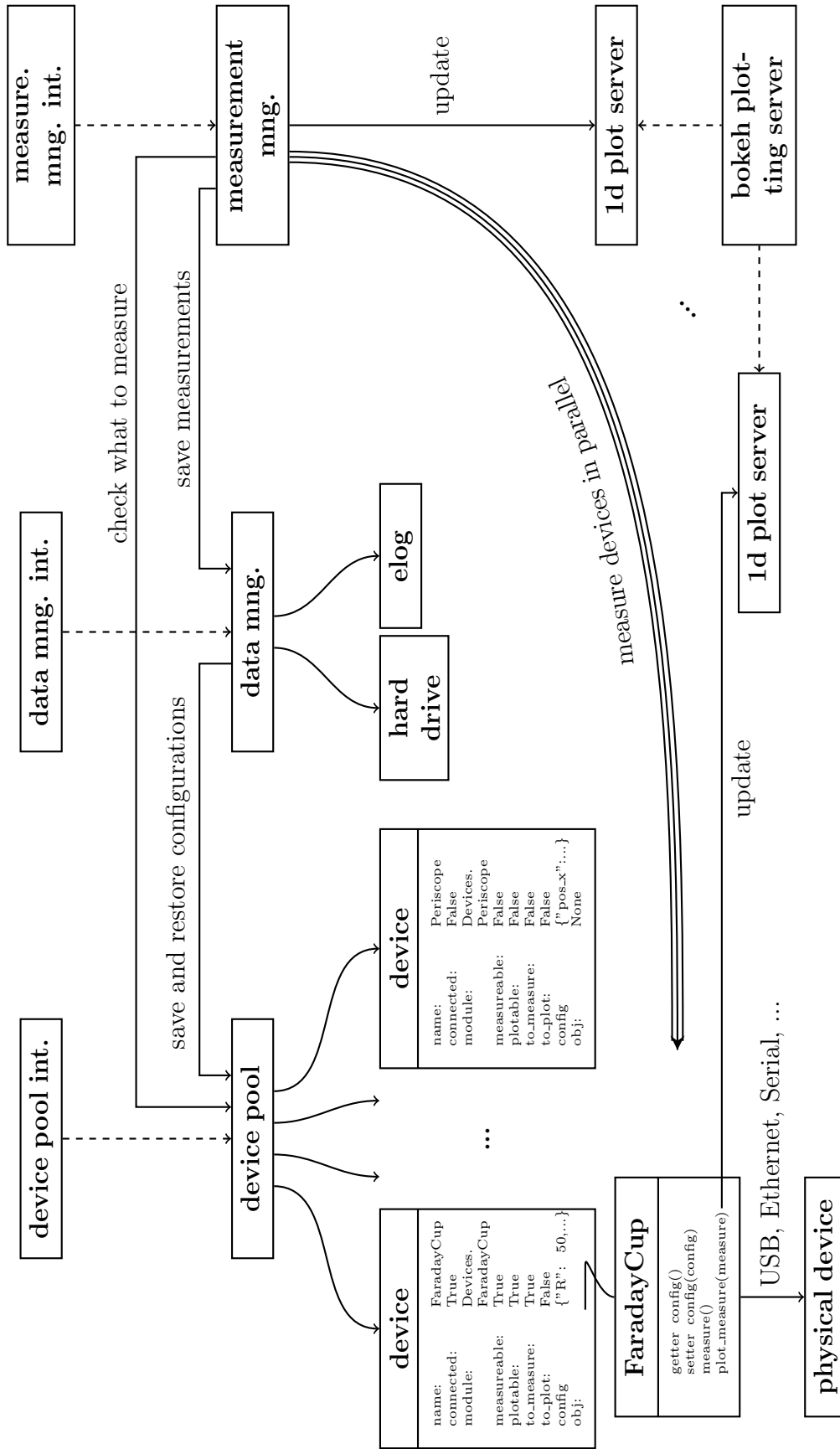


Figure 18: Structure of python based experiment control software. The dashed lines indicate where the regular user interfaces the software.

`to_measure = True`. The parallelization is needed in order not to have timing issues. Finally, the data manager deals with the storage and recovery of configurations and measurements on either the elog [23] or the hard drive. During measurements the data can be visualized live with bokeh plotting servers. They consist of permanently running python processes with the purpose to show the data fast over the browser. The three main classes each come with a graphical user interface (GUI) based on `ipythonwidgets`.

File Structure A pyPECS project is saved in a project folder (here `lwfserver`). The folder contains the main jupyter notebook (`NotebookGUI.ipynb`) and three sub-folders (`Devices`, `Data`, `Scripts`). As the name of the folders suggests, they contain the device related python files, the data taken in experiments and the main scripts that define the structure. As a regular user only the files in the data and device folder have to be modified.

How to Add a New Device As mentioned in the last paragraph, all the files specific to the individual devices are stored in the `Devices` folder. Each of the files follow a structure that allows the device pool to register devices and communicate with them. In the appendix the content of an example device file (`test_device1.py`) is listed (see Section 7.4.3). For all devices the file has to contain a class with the same name as the file, here `class test_device1`. The constructor (`def __init__(self, config, Other Devices to link)`) is called to connect the device. So all the communication to the devices should be initialized here. The `config` contains the configuration that should be applied to the device as it is connected. Each of the files also contains a dictionary called `default_config`, which should be specified. The last property that every device has to have is the `config` property (setter and getter). It is used to change and request the current configuration. In case a device can be measured a `measure` and `plot_measure` function have to be added. Usually the bokeh servers are used to plot the data, but also matplotlib can be used for inline notebook previews. Also, so-called special functions can be implemented. These begin with `spec_`. They are especially useful when dealing with the GUI because these functions appear as buttons in the device pool interface. A nice application for example is the special function `spec_align` in the `ParabolicMirror.py` file of the `lwfserver` project. It allows the alignment of the parabolic mirror with a single button click.

4 Tunable Permanent Magnet Elements

In order to focus and deflect the electron beam, tunable permanent magnet dipoles and quadrupoles (see Section 3.4) were developed. In short, the idea is to place magnets

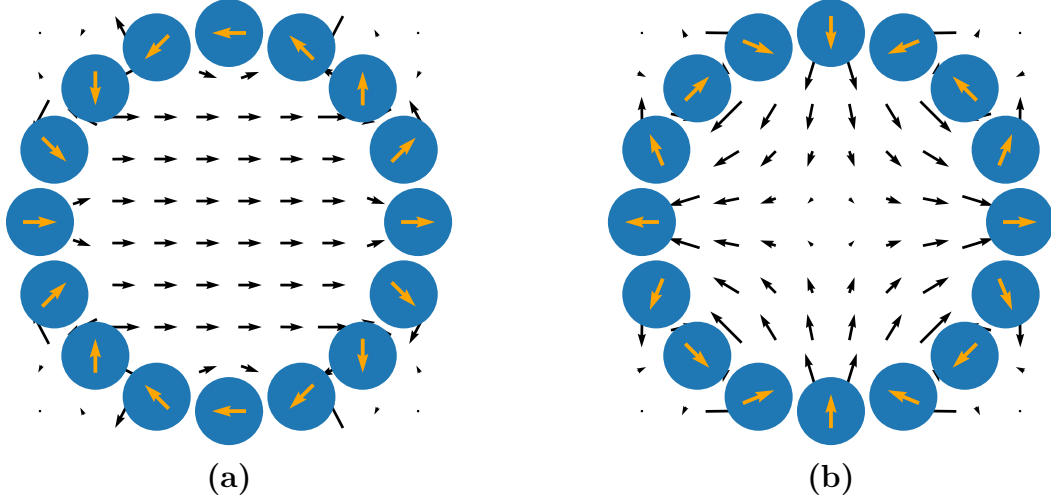


Figure 19: Visualization of the 2D model magnetic field (black arrows) of a dipole (a) and a quadrupole (b) Halbach array with diametrically magnetized rods (blue circles). The direction of magnetization is indicated by the orange arrow.

around the beampipe so that inside, quadrupole or dipole fields are generated. A ring of permanent magnets is called Halbach array (see Section 4.1). Depending on how the magnetization of the individual permanent magnets is oriented, the field inside the pipe changes (see Figure 19). In the device presented in this thesis, the magnetization direction of the individual magnets can be changed freely. This allows for field optimization (see Section 4.3) and, based on the same design, multipole magnets up to an octupole can be built (see Section 4.2). Because we do not use electromagnets, we cannot tune the

Aperture	5 cm
Length	8 cm
Maximal Integrated Gradient (QP)	0.117 T
Minimal Integrated Gradient (QP)	0.001 T
Maximal Mean Field (DP)	47.9 mT
Minimal Mean Field (DP) ^a	0.5 mT

Table 2: Summary of magnet element's measured properties for both the dipole (DP) and the quadrupoles (QP).

^aThe minimal mean field of D1 had to be guessed because the software that rotates the magnet rings had a bug, when the field maps were measured. The value has been guessed by looking at the results of the magnets Q1 and Q2.

magnetic flux by changing the current through the coils. Because the permeability μ_r of the material used for permanent magnets (SmCo) is close to unity, the superposition principle can be applied. It can easily be seen that the sum of 2N-pole fields around the same center results again in a 2N-pole field with different orientation and magnitude. So if two Halbach rings are placed concentrically around each other and the orientation of each individual ring is changed, the direction as well as the strength of the resulting magnetic field can be modified (see Figure 20) [6].

Mechanical Realization When dealing with permanent magnet installations only materials with a specific permeability μ_r close to unity should be used. At the same time, these materials have to be very robust because of the strong forces between the magnets. We used Samarium Cobalt Magnets (grade RECOMA 35E [19]) in our experiment. These are not as strong as Neodymium magnets, but are more resistant to temperature and radiation. In order not to fracture the fragile material, the magnets have been embedded in an aluminum casing (see Figure 21b).

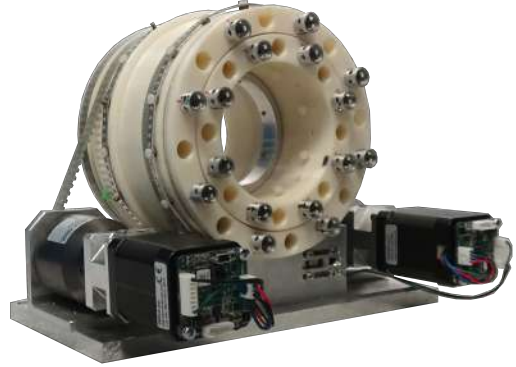


Figure 20: Image of the finished tunable permanent magnet element for the focusing magnet $Q2$.

The two Halbach arrays (inner and outer ring for tunability) are built by mechanically fixing the magnets in a 3D printed structure made of acrylonitrile butadiene styrene (ABS). The two rings are designed so that a sliding contact bearing allows for rotation. The outer ring is pushed on a sliding contact bearing which is connected to the aluminum base blade. Two stepper motors (Trinamic PD42-4-1140-TMCL) that are connected to a planetary gear (Neugart PLPE 5020/OP2) deliver a torque of up to 14 N m. The shafts of the gears are connected to the Halbach rings by V-belts. The gear reduction from the shaft of the planetary gear to Halbach ring rotation is 1/5. With the resulting torque it was possible to overcome the force between the magnets (see Figure 21a) and the friction of the two sliding contact bearings (between rings and base blade). The motors can be controlled with the TMCL interface over a RS-485 serial bus. In fact, all the motors for the quadrupoles and dipoles can be driven by a single bus which is connected to the computer with a serial-to-usb adapter.

In the following Sections we are going to elaborate the ideas behind the permanent magnets. After giving a short introduction to Halbach's idea of constructing permanent magnet arrays for charged particle beam focusing elements (see Section 4.1), analytic expressions for important properties like magnetic field and torque (see Section 4.2) are derived in 2D. This allows the modelization of the optimization process (see Section 4.3). Finally, the results obtained from a rotation coil and field map measurement are presented (see Section 4.4).

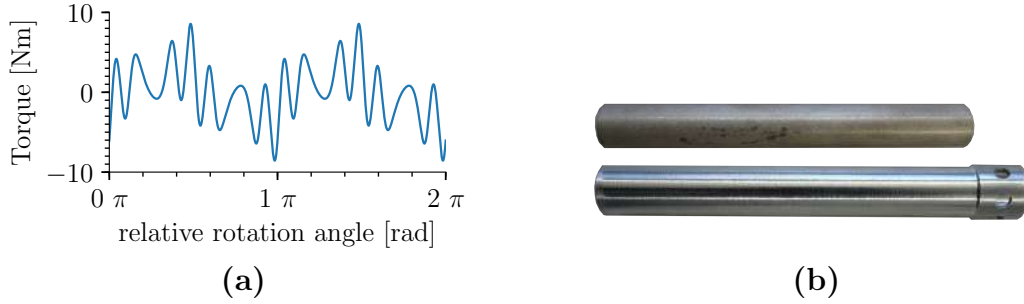


Figure 21: *Properties of the mechanical design. In graph (a) the torque between the Halbach rings is plotted. This result is based on the calculation in Section 4.2. Image (b) shows the permanent magnets with and without casing. The holes on the right side of the casing allow for rotation during the optimization process (see Section 4.3).*

4.1 Halbach Arrays

The design idea of permanent magnet multipoles for accelerator applications goes back to the work of Halbach [10]. He showed that a cylindrical ring of permanent magnets magnetized in the direction

$$\vartheta = (N + 1) \varphi$$

will generate a $2N$ -pole field around the center. In his paper Halbach derived an analytic

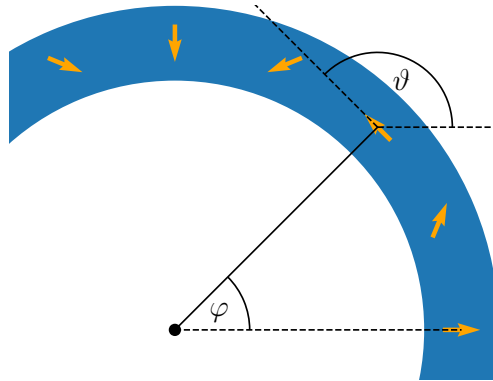


Figure 22: *Direction of magnetization (orange arrows) in continuous Halbach array of permanent magnets (blue). Here the configuration of a quadrupole is shown ($N = 2$).*

expression for the $2N$ -pole field of an infinitely long cylinder

$$B^*(z_0) = \left(\frac{z_0}{r_1}\right)^{N-1} B_r \frac{N}{N-1} \left[1 - \left(\frac{r_1}{r_2}\right)^{N-1}\right]$$

with B_r being the material specific remnant field and r_1 , r_2 being the inner and outer radii of the cylinder shell. Here complex coordinates are used to describe the 2D vector field. Halbach proposed in his paper that such a continuously varying magnetization can be approximated by an cylindrical array of wedges which are each homogeneously magnetized, called the Halbach array. He showed that such an array also generates a multipole moment, but with weaker magnitude.

4.2 2D Analytic Expressions for Magnetic Field and Torque

In this Section we extend and summarize the theoretical results that are presented in detail in [10]. The article by K. Halbach and S.M. Lund gives a nice introduction into the problem [18]. The relationship between the magnetic flux density B and the magnetic field strength H are, in a permanent magnet setup without ferromagnetic components ($\mu_r - 1 \approx 0.01$), well approximated by

$$B = B_r + \mu_0 H,$$

where B_r is the remnant magnetic field and $\mu_0 = 4\pi \times 10^{-7} \text{ Vs}/(\text{Am})$ the vacuum permeability. Analytic calculations of the magnetic field generated by permanent magnets are rather simple because, given that $\mu_r = 1$, the superposition principle can be applied. Using Maxwell's Equations ($\nabla \times H = 0$, $\nabla \cdot B = 0$), the following set of equations can be derived

$$\begin{aligned}\nabla \times B &= \nabla \times B_r \equiv \mu_0 j \\ \nabla \cdot B &= 0.\end{aligned}$$

In 2D these equations reduce to

$$\begin{aligned}\partial_x B_y - \partial_y B_x &= j_z \\ \partial_x B_x + \partial_y B_y &= 0,\end{aligned}$$

which can be simplified to a Poisson's Equation for A_z ($B_x = \partial_y A_z$, $B_y = -\partial_x A_z$), where A_z is the z component of the vector potential in \mathbb{R}^3

$$\nabla^2 A_z = -\mu_0 j_z.$$

Using the Green's function of the Laplacian in 2D, given by $G(r) = \frac{1}{2\pi} \log(|r|)$, the solution for the potential A_z can be integrated as

$$A_z(r_0) = -\frac{\mu_0}{2\pi} \int_{\mathbb{R}^2} dx dy j_z \log(|r_0 - r|).$$

This leads to the following solution for B which takes a particularly simple form when \mathbb{R}^2 is identified with \mathbb{C}

$$\begin{aligned}\vec{B}(r_0) &= -\frac{\mu_0}{2\pi} \int_{\mathbb{R}^2} dx dy \frac{j_z}{|r_0 - r|^2} (y_0 - y, x - x_0)^T \\ &\underbrace{\implies}_{\mathbb{R}^2 \equiv \mathbb{C}} B^*(z_0) = \frac{\mu_0}{2\pi i} \int_{\mathbb{R}^2} dx dy \frac{j_z}{z_0 - z}.\end{aligned}\tag{4.2.1}$$

The identification with \mathbb{C} is $r = (x, y)^T \rightarrow z = x + iy$. Here the asterisk (*) denotes complex conjugation. Equ. (4.2.1) is very powerful because with tools from complex analysis it offers a very simple method to calculate the magnetic field.

Field of Infinitely Long Diametrically Magnetized Cylinder Since our design of the tunable permanent magnets is based on diametrically magnetized rods, we will only derive an expression of the field for this special case. We assume that the rods have a constant B_{r0} in the bulk which is taken without loss of generality to be oriented along the x axis. Therefore, the remnant magnetic field can be expressed as

$$\vec{B}_r = B_{r0} \theta(R - r) \vec{e}_x,$$

where θ is the Heaviside function. From this we can calculate the current density as

$$\mu_0 j_z = \partial_x B_{ry} - \partial_y B_{rx} = B_{r0} \delta(R - r) \frac{y}{r}. \quad (4.2.2)$$

Now we can evaluate the integral in Equ. (4.2.1) as

$$\begin{aligned} B^*(z_0) &= \frac{B_{r0}}{2\pi i} \int_0^{2\pi} \int_0^\infty d\varphi r dr \delta(r - R) \frac{\sin(\varphi)}{z_0 - r e^{i\varphi}} \\ &= -\frac{B_{r0} R}{4\pi} \int_0^{2\pi} d\varphi \frac{e^{i\varphi} - e^{-i\varphi}}{z_0 - R e^{i\varphi}} \\ &= -\frac{B_{r0}}{4\pi i} \int_{S_1} du \frac{u^2 - 1}{u^2(z_0/R - u)} \\ &= -\frac{B_{r0}}{2} \sum_{|a| < 1} \text{Res}(a, \frac{u^2 - 1}{u^2(z_0/R - u)}). \end{aligned}$$

By identifying the integral with a complex contour of a meromorphic function, the problem was simplified to finding the residues of a complex function. The residues are

$$\begin{aligned} \text{Res}(z_0/R, \frac{u^2 - 1}{u^2(z_0/R - u)}) &= -\frac{z_0^2 - R^2}{z_0^2} \\ \text{Res}(0, \frac{u^2 - 1}{u^2(z_0/R - u)}) &= -\frac{R^2}{z_0^2}. \end{aligned}$$

Differentiating the two different cases ($|z_0| > R$ and $|z_0| \leq R$) leads to

$$B^*(z_0) = \frac{B_{r0}}{2} \begin{cases} 1 & , |z_0| \leq R \\ \frac{R^2}{z_0^2} & , |z_0| > R \end{cases}. \quad (4.2.3)$$

The field depletes with the square of the distance to the magnet center. This is expected since the field of a single wire depletes like $1/d$ and we made a dipole out of it (see Equ. (4.2.2)). Next, we would like to calculate the multipole moments around the origin when the magnet is placed at z_c . To extract the multipole moments, we have to write Equ. (4.2.3) in terms of a power series in $z = z_0 + z_c$. The coefficients of the series are then the multipole moments. From here on, we will assume that the rod is magnetized in a direction at the angle φ with respect to the real axis. Therefore B_{r0} has to be multiplied by $e^{i\varphi}$. Because we are only interested in the field outside the magnets, we will from now on only consider the case $|z_0| > R$. Then the field generated around the origin by a

magnet placed at z_c can be expressed as

$$\begin{aligned} B^*(z - z_c) &= \frac{B_{r0}}{2} R^2 e^{i\varphi} \frac{1}{(z - z_c)^2} \\ &= \frac{B_{r0}}{2} R^2 e^{i\varphi} \sum_{n=1}^{\infty} n \frac{z^{n-1}}{z_c^{n+1}}, \end{aligned}$$

where in the last step we used the derivative of the geometric series with respect to $z < z_c$. The definition of the multipole moments around the origin is given by⁷

$$B^* = \sum_{n=1}^{\infty} b_n(0) z^{n-1}.$$

Therefore we find for the moments

$$b_n(0) = \frac{B_{r0}}{2} R^2 e^{i\varphi} n \frac{1}{z_c^{n+1}}.$$

Field of an Array of Infinite Diametrically Magnetized Cylinders Using the results of the last paragraph, in particular the analytic expression of the multipole moments outside an infinite diametrically magnetized cylinder centered at z_c , the calculation of the multipole moments of an array of magnets is straightforward. We will introduce M equally spaced magnets positioned at a radius r around the origin. Their centers have the coordinates $(z_c)_m = r e^{i\frac{2\pi}{M}m}$ and their magnetization is oriented with an angle $\varphi_m = (N + 1)\frac{2\pi}{M}m$. In this case the multipole moment can be expressed as

$$\begin{aligned} b_n(0) &= \frac{B_{r0}}{2} \frac{R^2}{r^{n+1}} n \sum_{m=0}^{M-1} \exp\left(2\pi i [(N + 1) - (n + 1)] \frac{m}{M}\right) \\ &= \begin{cases} \frac{B_{r0}}{2} \frac{R^2}{r^{N+1}} N M & , \text{ for } N = n \\ 0 & , \text{ elsewhere.} \end{cases} \end{aligned} \quad (4.2.4)$$

Torque of Two Infinite Diametrically Magnetized Cylinders The calculation of the magnetic field showed that in 2D many properties of the magnetic rods can be calculated analytically. To estimate the size of the motors that turn the rings, the torque that one rod exerts on another has to be calculated. The magnetization of the rods are oriented at angles α and β from the x -axis (see Figure 23). The distance between the two rods is d . The origin of the coordinate system was chosen to be the center of the magnet (with angle β) on which the force is acting. Using complex notation⁸, the torque τ per

⁷Sometimes the multipole moments are split in real and imaginary part, rotated by (-i) in the complex plane and normalized by the radius of the beam pipe r_0 . Then b_n has to be replaced by $-i(a_n + ib_n)/r_0^{n-1}$. Here we will not use this convention.

⁸

$$\begin{aligned} A \times B &\rightarrow \text{Im}(a b^*) \\ A \cdot B &\rightarrow \text{Re}(a b^*) \end{aligned}$$

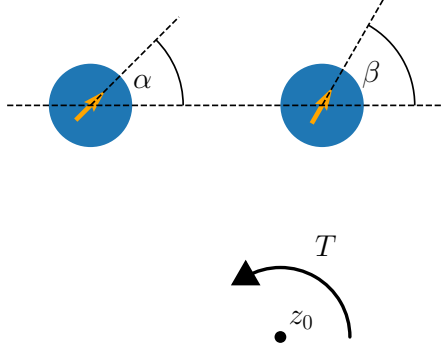


Figure 23: Coordinate system for the torque calculation. Direction of magnetization (orange arrows) of permanent magnets (blue).

length can be calculated as

$$\begin{aligned}
\tau &= \int_{\mathcal{C}} \text{Im}((z - z_0) f^*) \, dx \, dy \\
&= \int_{\mathcal{C}} \text{Im}((z - z_0) (ij_z B)^*) \, dx \, dy \\
&= - \int_{\mathcal{C}} j_z \text{Re}((z - z_0) B^*) \, dx \, dy \\
&= - \frac{1}{2\mu_0} B_{r_0}^2 R \int_0^{2\pi} \int_0^\infty \delta(R - r) \text{Im}(e^{i(\varphi - \beta)}) \text{Re}\left(e^{i\alpha} \frac{e^{i\varphi} - z_0/R}{(e^{i\varphi} + d/R)^2}\right) dr \, d\varphi \\
&= \dots = \frac{\pi}{4\mu_0} B_{r_0}^2 R \sum_{|a| < 1} \text{Res}\left(a, \frac{e^{-i\beta} u^2 - e^{i\beta}}{u^2} \left[e^{i\alpha} \frac{u - z_0/R}{(u + d/R)^2} + e^{-i\alpha} \frac{1/u - z_0^*/R}{(1/u + d/R)^2} \right] \right) \\
&= - \frac{\pi}{2} \frac{B_{r_0}^2 R^3}{\mu_0 d^3} (2 \text{Im}(z_0 e^{i(\alpha - \beta)}) + d \sin(\alpha + \beta)),
\end{aligned}$$

where f is the Lorentz force in complex notation ($j \times B = j_z(-B_y, B_x)^T \rightarrow ij_z B$). In the last step we had to calculate the residue of a complicated function. This was done using the sympy package (see Section 7.4.1). The total torque T is related to τ by $T = \tau L$, where L is the length of the magnet.

4.3 Optimization of the Magnetic Field

A difficulty when dealing with permanent magnets is the fluctuation of the strength B_r between the samples of about 2% [19]. This variation is due to the magnetization process and the purity of the material. In order to compensate for these fluctuations, additional degrees of freedom have to be introduced into the design. Halbach's original idea [10] of using wedges is very limited in this respect. One might think of adding a possibility to change the radius of the wedges. This is difficult to construct mechanically however. A more simple idea is to replace the wedges by cylindrical rods that are magnetized diametrically (see Figure 19). By changing the orientation of the individual rods, deviations in the magnetic field can be corrected.

By correction we understand minimizing the unwanted multipole moments. For the case of a quadrupole this means explicitly turning the magnets until all the multipole moments except the quadrupole moment vanish. In order to minimize the multipole moments efficiently, it is important to understand how the rotation of the magnet k changes the moments. To illustrate this, we repeat the calculation of Equ. (4.2.4), but consider that $\varphi_m = 2\pi \frac{m}{M} (N + 1) + \Delta\varphi_m$. This results in

$$b_n(0) = \frac{B_{r0}}{2} \frac{R^2}{r^{n+1}} n \sum_{m=0}^{M-1} \exp\left(2\pi i [(N + 1) - (n + 1)] \frac{m}{M} + i\Delta\varphi_m\right).$$

The change of $b_n(0)$ with respect to small $\Delta\varphi_k$ is

$$\left. \frac{\partial b_n(0)}{\partial \Delta\varphi_k} \right|_{\Delta\varphi_m=0 \text{ for } m=0\dots(M-1)} = i \frac{B_{r0}}{2} \frac{R^2}{r^{n+1}} n \exp\left(2\pi i [N - n] \frac{k}{M}\right). \quad (4.3.1)$$

Thanks to the above relations we were able to minimize the dipole, quadrupole, sextupole and octupole moments of the permanent magnet arrays manually. In Figure 25 one of the optimization results is displayed.

Optimization Procedure The following procedure was followed for each individual ring, inner and outer. This means that in total 8 optimizations had to be performed.



Figure 24: Image taken during the optimization of the magnetic field inside a Halbach ring. After each rotation of a magnet the field inside the ring was remeasured with the rotation coil (see Section 4.4).

n	α_m
1	$\pi/2 + \pi/4 m$
2	$\pi/2$
3	$\pi/2 - \pi/4 m$
4	$\pi/2 - \pi/2 m$
5	$\pi/2 - 3\pi/2 m$

Table 3: Direction of change of multipole moment in the complex plane. Specifically, this table shows the angle in the complex plane of Equ. (4.3.1). The values are for the special case of quadrupole magnet array ($N = 2$) with $M = 8$ magnets.

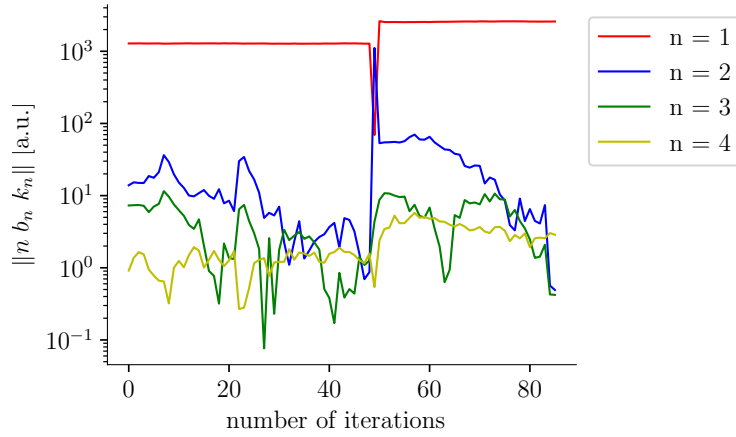


Figure 25: Convergence of the manual minimization of multipole moments (here quadrupole, sextupole and octupole) based on the example of the outer ring of the dipole magnet $D1$. k_n is the sensitivity of the rotating coil measurement (see Section 4.4) with respect to the n th multipole moment [3, 2]. After 51 iterations the number of magnets in the ring was increased from 4 to 8.

For simplicity (reduction of degrees of freedoms) initially only 4 magnets were put in the ring (inner or outer). Afterwards, the magnetic field moments were measured with the rotating coil. Depending on the result, the orientation of the magnets was changed (see directions in Table 3). Then 4 additional magnets were inserted and optimized by the same method.

4.4 Characterization of the Magnetic Field

The magnets have been characterized using two types of measurements, a rotating coil measurement that extracts the 2D multipole moments of the magnets and a field mapping that can measure the shape of the fringe fields.

Rotating Coil Measurement As the name suggests, a rotating coil is a coil that is rotated by a motor in a magnetic field. The induced currents allow the reconstruction of the strength and orientation of the multipole moments around the center of rotation [3, 2] which was chosen to be the center of the Halbach ring. Depending on the desired accuracy,

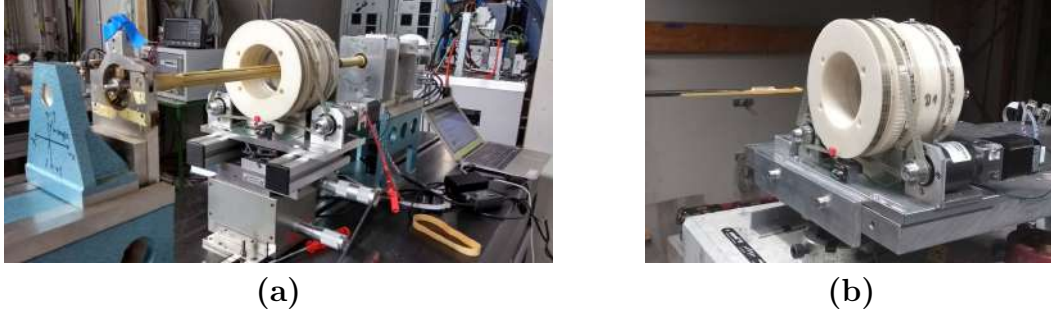
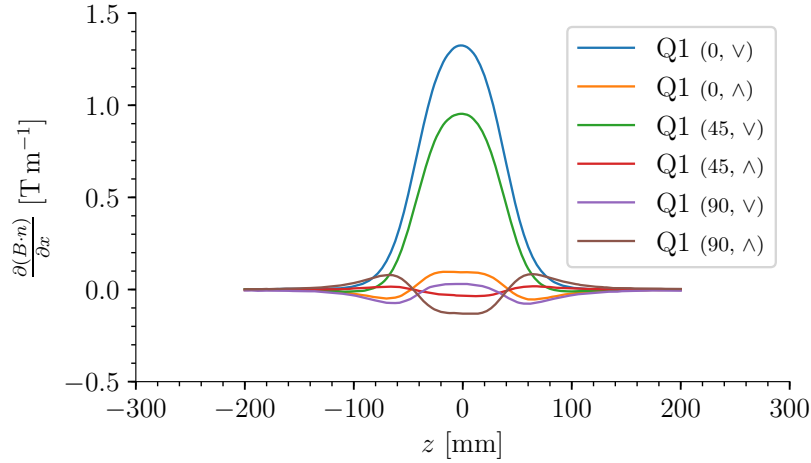


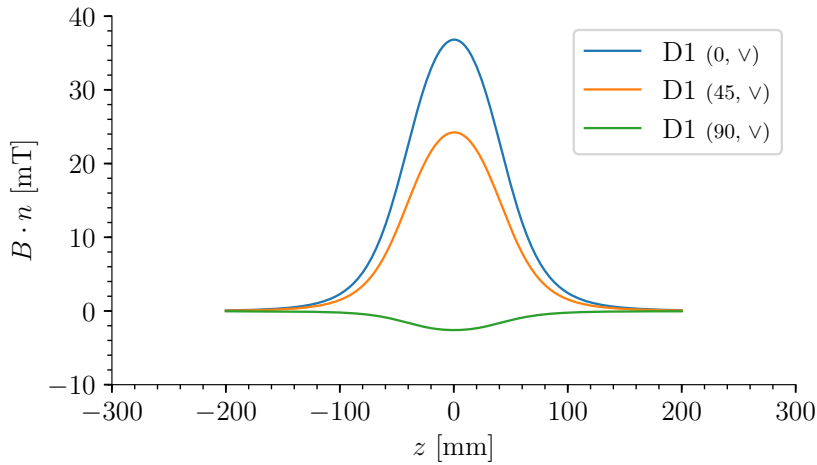
Figure 26: *Images of measurement setups for characterization of the magnetic field inside the lattice elements. Image (a) shows the rotating coil setup and image (b) the hall probe measurement.*

each measurement took from 6 s to 10 s. This allowed for large parameters sweeps and optimizations. This method was used for both the characterization of the tunability (see Figure 36 in Appendix 7.2) and the minimization of the unwanted multipole moments (see Section 4.3). To measure the results shown in Figure 36 the outer ring was rotated by 360° in 4° steps. After each step a rotating coil measurement was made. The accumulated data was used to calibrate the strength and orientation of the magnetic field with respect to the motor position. The results show that by rotating the rings the orientation and magnitude of the multipole moments can indeed be changed. The data of the quadrupoles shows a large dipole component. This problem is due to alignment. If the rotating coil is not at the center of the ring, the quadrupole component of the field will lead to an increase in the dipole component. The superposition of a pure quadrupole field with a pure dipole field is a pure quadrupole field with the same gradient, but around another center. Therefore, if the two quadrupole rings, aligned mechanically by the sliding contact bearing (see Figure 20), do not share the same magnetic center, the resulting field will also have relatively high dipole components. This component changes depending on the orientation of the two rings. However, for the dipole this is not a problem (see Figure 36a). Dipoles do not have a magnetic center and therefore the resulting field is not crucially dependent on the alignment of the two magnet rings.

Hall Probe Mapping The rotating coil measurement has two issues. First it can only measure 2D multipole moments and second the calibration of the rotating coil requires a magnet, whose multipole moments are known precisely. To solve these problems, several Hall probe scans were performed. In Figure 26a one can see the setup of the experiment. A Hall probe that can be moved in the 3 spatial dimensions is moved in the gap of the Halbach ring where it measures the magnetic field component in the y -direction (perpendicular to the base blade of the magnet). For three magnets (Q1, Q2, D1) measurements for different absolute angles (0° , 45° , 90°) at two different relative angles (field minimum, field maximum) were made. For each of these 12 configurations a field map of 21×201 (x and z respectively) measurements was taken. Each measurement took 20 min. The y -coordinate of the probe in the vertical center of the Halbach ring was during the whole measurements. In Figure 27a the gradients of the Q1 magnet for the different configurations is displayed. One can clearly see that when the magnet elements are tuned to



(a)



(b)

Figure 27: Gradients and fields on axis ($y = 0$ mm) for the magnets Q1 and D1 at different absolute angles (0° , 45° , 90°). The symbol \wedge stands for the maximal field strength and \vee for the minimal.

minimum 2D quadrupole component, the gradient of the magnetic field in transverse direction isn't zero. Rather the integral of the gradient along z becomes zero. The gradient's dependence on z reminds one of a symmetric quadrupole triplet. The reason for this lies in the design of the rings. When optimizing the field with the rotating coil, the 2D quadrupole component of each of the rings was tuned to the same value. For the larger rings however, the fringe fields extend further in the z -direction. So when the fields of two rings with the same mean gradients are subtracted from each other (superposition), only the mean gradient is zero. For large z the field of the outer ring and for smaller z the field of the inner ring is dominating. This phenomenon is what forms the quadrupole triplet-like field. In the case of a dipole a similar picture can be applied which leads to the conclusion that for low mean field configurations the z profile resembles the one of a dipole triplet.

4.5 Electron Equivalent of a Deformable Lens

As seen in Section 4.4, with the two-ring design, the 2D multipole moments could be tuned down to a percent level of their maximal value. However, once the magnet rings are optimized (see Section 4.3) the configuration of each of the rings can't be changed anymore. This means that once the magnet is installed in the accelerator, a 2N-pole magnet stays a 2N-pole magnet. If, instead of motorizing the two magnet rings, each of the orientations of the permanent magnets could be changed independently, the strength and orientation of more than just one multipole component could be set. For 8 magnets one would be able to choose different values for all moments up to the octupole component. This would then allow for beam shape optimization as done in optics with deformable mirrors or lenses. This optimization would be interesting in the field of fixed field accelerators, where non-tunable permanent magnet beamlines are used to transport charged particles. The insertion of some deformable electron lenses into the beamline would allow to correct for ageing effects of the permanent magnets.

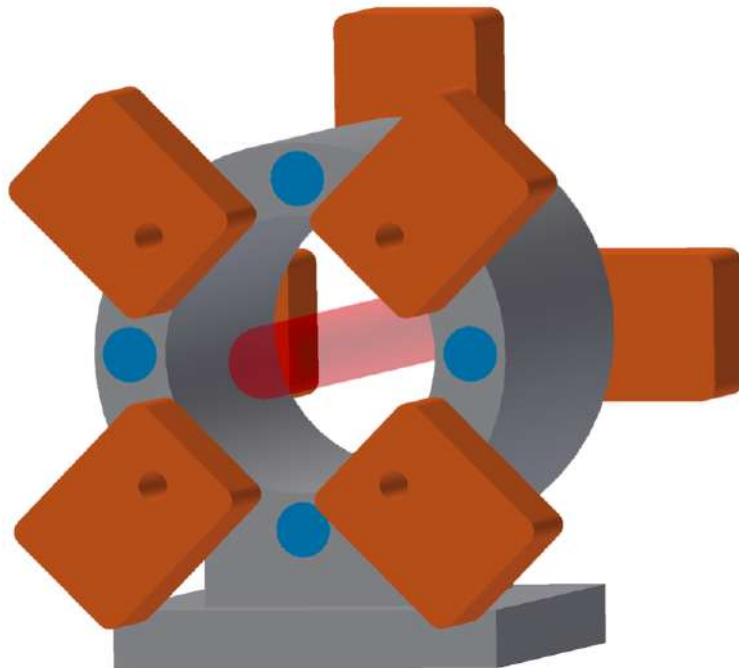


Figure 28: *3D sketch of deformable electron lens. The motors (orange) turn eight diametrically magnetized permanent magnet rods (blue). Using this technique the field inside the beam pipe (red) can be optimized.*

5 Characterization of the Electron Bunches

For the characterization of the generated electrons, several experiments have been conducted. It has been verified that electrons to energies above 32 keV were accelerated. The entire accelerator was characterized using the signal of the Faraday cup (FC). As described in Section 3.3, diagnostics tools based on scintillating materials like a screen and a fiber were used, but no signals correlated to the laser pulse could be observed.

The data presented in the following parts were collected on two different measurement days. On these days the signals on the Faraday cup showed features that could be correlated to wake field generation, X-ray generation and electron acceleration. On both days the diagnostics cross (right chamber in Figure 6) was mounted directly behind the acceleration chamber (central chamber in Figure 6). Between the two experimenting days three changes were made to the experimental setup. First, the puppet of the gas jet that closes the valve was changed. Second, the blade that introduces a shock in the gas flow was electrically grounded by a thin copper wire (see Figure 35b). However, the major change was the shielding of the Faraday cup. As described in Section 3.3, aluminum foil covers the front of the FC to avoid detecting signals coming from either the laser light or other low frequency electro-magnetic waves generated in the plasma. On the first of the two days, this shielding did not entirely cover the FC. Therefore, not only electrons and X-rays, but also radio frequency (RF) waves could enter the housing of the FC, meaning that it was operating as an antenna or pickup. On the second day the FC shielding was improved, so no RF could be measured. The day the FC was not properly shielded will be referenced as day 1 (d1). The second day will be referenced as day 2 (d2).

Correlation of Signal to Gas Jet and Laser As a first step of the experiment, we verified that the signal measured on the FC was coming from a process that involves both the laser and the gas. To test this, the gas jet, the laser or both were switched off. In all three cases the signal completely disappeared suggesting that whatever is measured comes from the interaction between the gas and the laser.

5.1 Typical Features of Faraday Cup Signals

During the measurements different characteristic types of signal were observed. The shape of the signal varied depending on the configuration of the experiment. In Figure 29 some of the possible different shapes are shown.

Day 1 Figure 29a shows a signal that is very typical for day 1. The positive peak of the signal disappeared when a strong permanent magnet was held directly on the FC. Therefore, the signal must come from low energy electrons that are extracted from either the aluminum foil or the FC. This process could possibly be due to X-rays. However, if the magnet was held on the beampipe, the integral of the signal disappeared, but the positive peak remained. This supports the theory that the total negative integral is due

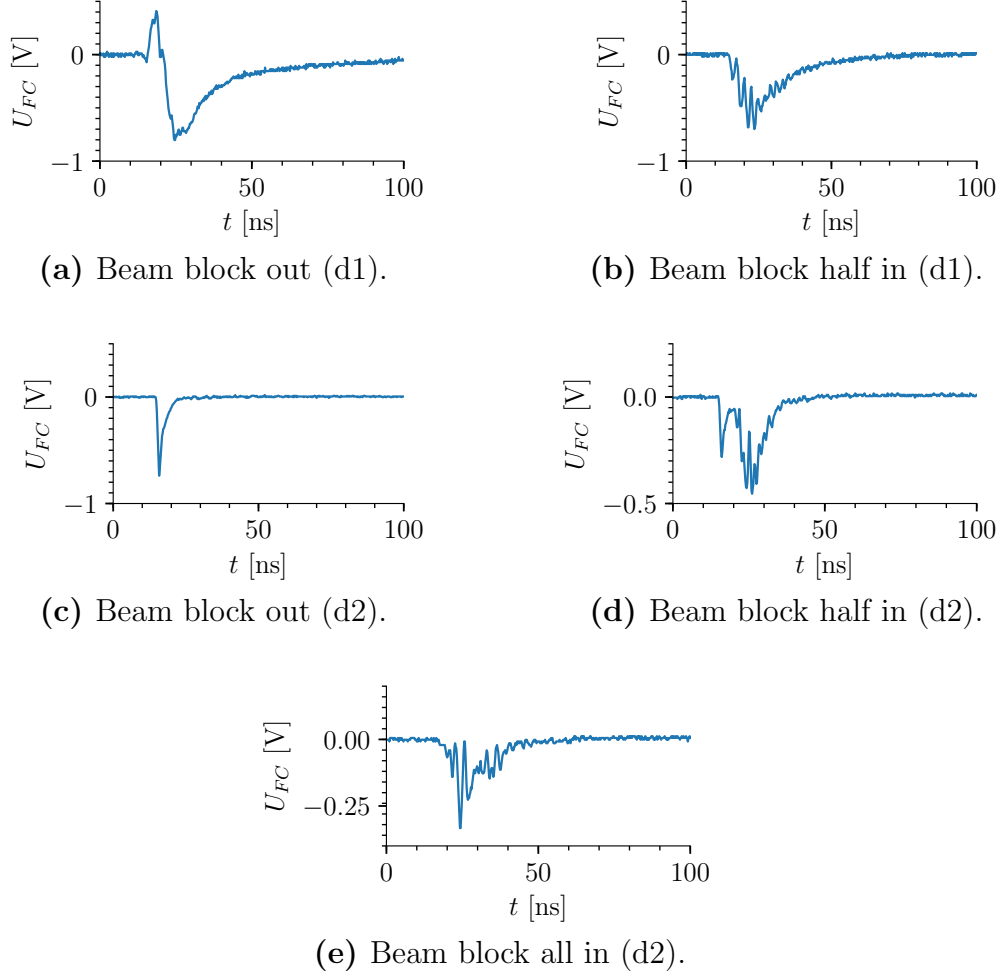


Figure 29: Typical Faraday cup signals observed on day 1 and day 2, with and without the beam block. The beam block was used for the beam size measurement (see Section 3.3 and 5.3).

to charged particles that traveled through the beampipe with which the positive peak in the front is not correlated. As a third test, the FC was mounted on one arm of the diagnostics cross that is perpendicular to the propagation direction of the laser pulse (see Figure 13b). No generated electrons can reach this position because they would either have to change direction or fly through the walls of the beampipe. These are both very unlikely because energies up to 200 keV are expected from the laser parameters (see Section 2.2). Mounted at this position, the FC did not show the positive feature (see Figure 29a). Combining this with the results of the magnet test, this suggests that the positive peak comes from something uncharged propagating along the laser axis. This could be X-rays. Additionally, like with the magnet, the integral of the signal vanished. This shows that in this configuration only the RF wake fields generated by the electron bunches were measured, which supports the possibility that the Faraday cup was operating as a pickup antenna.

Day 2 The graph shown in Figure 29c is typical for day 2. The signal was very short and showed a single peak. The sudden rise (1 ns) accompanied with an exponential decay ($\tau_{\frac{1}{2}} = 1$ ns) are expected when a short electron bunch is hitting the FC, because then the FC behaves like a capacitor which is discharged over the 50Ω resistor of the preamplifier. Also, when a magnet was held at the beampipe, the signal completely disappeared. Thus, we conclude that the peak signal must come from electrons travelling through the beampipe and hitting the FC. To be detected by the FC, the electrons have to pass through one layer of aluminum foil with a thickness of $10\mu\text{m}$. Therefore, they must have kinetic energies above 32keV [13].

5.2 Dependence of FC Signals on the Accelerator's Configuration

As discussed in the last Section, the signals of the two measurement days showed different features. In this Section, the way these features depended on the configuration of the accelerator is discussed. The coordinates x , y and z describe the position of the laser focus with respect from the nozzle. x is measured parallel to the gas jet (up \rightarrow down in experiment) and z parallel to the laser pulse's propagation. The origin of this coordinate system is chosen to be centered on the gas jet at a distance of 0.5mm to the nozzle. This is the minimal distance allowed so the laser doesn't hit the blade (see Section 3.2). For both days the same coordinate system is chosen.

As described in Section 2.2, the injection process depends on the density down-ramp (DDR). Therefore, if the observed signals come from DDR injection, they should strongly depend on z . Only if the focus of the laser is on the DDR, should a signal be observed. The DDR being very short ($\sim 10\mu\text{m}$) and the Rayleigh length of the laser's focus being of the order of 0.3mm , the signals should only appear within a range of $\pm 0.2\text{mm}$ of the position of the shock front.

Day 1 The plots in Figure 30 show how the charge Q , which is proportional to the negative integral of the signal (see Figure 29a), depended on both the position of the focus (y , z) and the gas jet's backing pressure P . The z dependence of the charge was almost flat (see Figure 30b). Therefore, the process generating the signal on the FC was not due to electrons being accelerated after the DDR position. As the signal decreases as a function of y and increases with backing pressure P , it seems that the process was proportional to the gas density. This behavior is similar to the one observed by Benedikt Hermann in his master thesis [13]. As he explains, when the backing pressure exceeds 4.5MPa , the valve of the gas jet doesn't open properly anymore. Therefore, the two measurements at $P = 4.5\text{MPa}$ and $P = 5.0\text{MPa}$ have to be discarded.

Day 2 Contrary to day 1, the measured charge Q depended strongly on the z position (see Figure 31a). After starting the experiments on day 2, it took an extensive search to find a configuration where significant charge ($> 0.1\text{pC}$) was measured on the FC. This is a clear indication that the process responsible for the signal on the FC is related to electrons accelerated at the DDR.

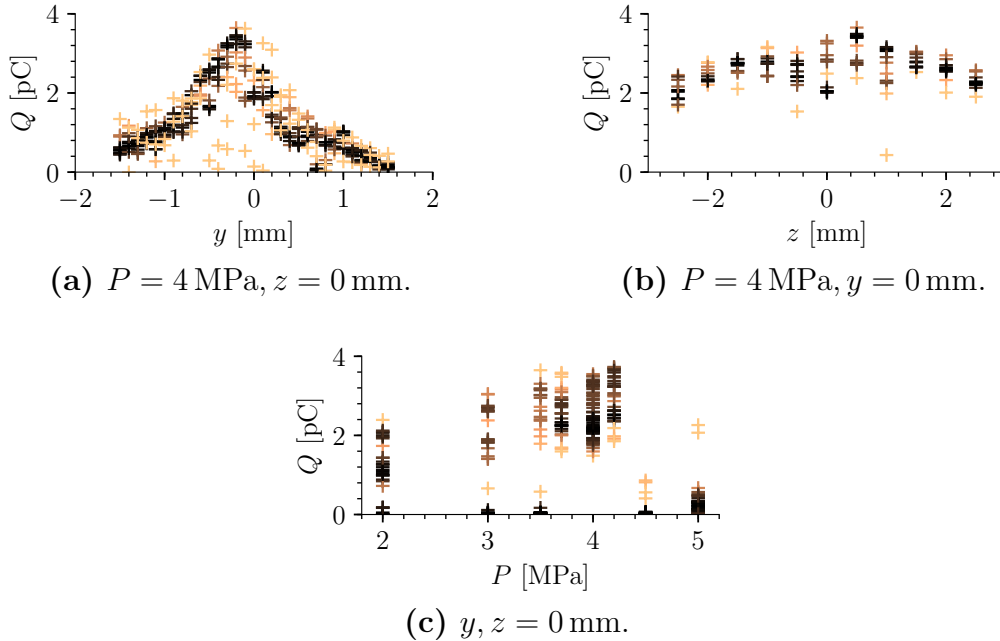


Figure 30: Charge on FC for different experiment parameters during day 1. For all the measurements $x = 0$ mm. One cross corresponds to one laser shot on the gas jet. The color of the crosses indicates the density of data points for a specific accelerator configuration as a function of the charge Q (black: high density, orange: low density). The density is calculated by the `KernelDensity` function in the `scikit-learn` package [22]. The following plots that use the copper colorbar are based on the same principle.

Figure 31b shows that the accelerated charge Q depended on the laser pulse length $c\tau$. For $P = 3.5$ MPa the peak of the accelerated charge was at $z_{comp} = 37.425$ mm. However, for $P = 2.7$ MPa two peaks in charge can be distinguished ($z_{comp} = 37.400$ mm and $z_{comp} = 37.45$ mm). Such a behavior is typical for a resonant generation of the plasma wake. Let us assume that for $z_{comp} = 37.425$ mm the pulse length L_{min} was minimal⁹ and for $P = 3.5$ MPa the plasma wavelength matched the resonance condition $\lambda_p \approx 2.5L_{min}$. Then, for lower plasma densities ($P = 2.7$ MPa) the laser pulse length has to be increased to match the resonance condition again. As the laser pulse length increases in both directions from the optimum ($z_{comp} = 37.425$ mm), two peaks in the charge plot (see Figure 31b) are expected for $P = 2.7$ MPa. At this point we also note that this measurement should be repeated, in order to further increase the statistical evidence for the argument above, and to rule out that the two peaks observed are an artifact of the noise.

⁹This is reasonable because the length was optimized with the WIZZLER-DAZZLER loop for $z_{comp} = 37.400$ mm (see Section 3.1).

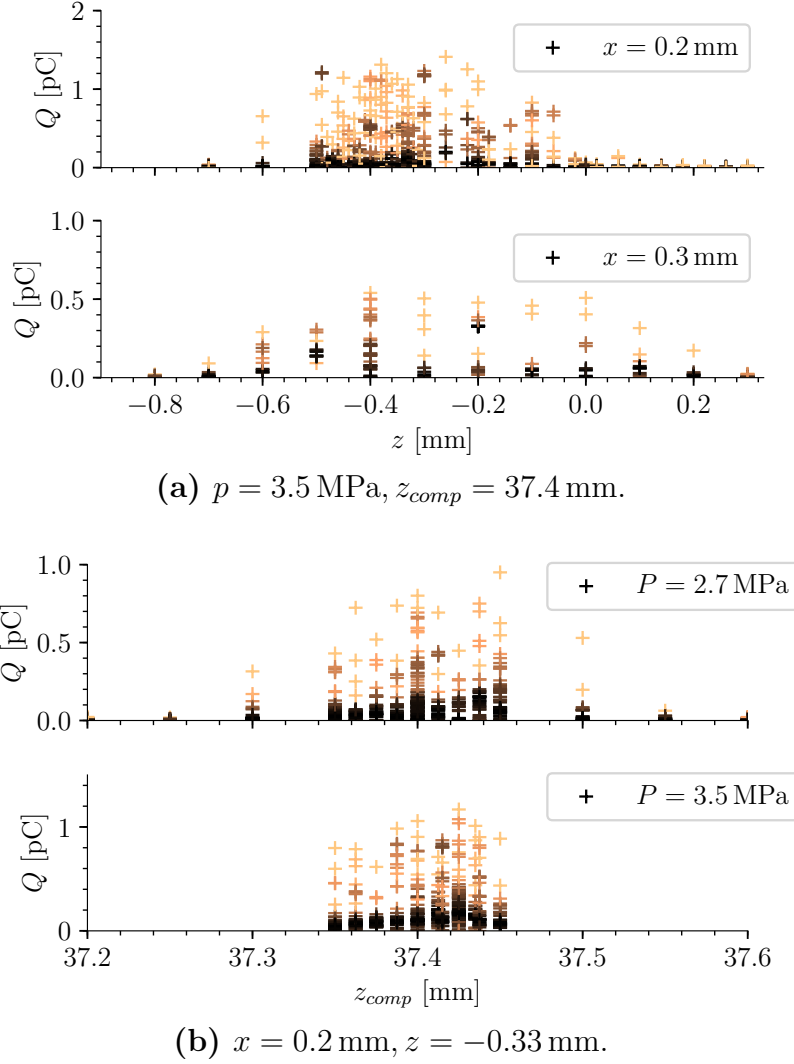


Figure 31: Charge on FC for different experiment parameters during day 2.

5.3 Beam Size Measurements

After optimizing the charge on the FC, further experiments were conducted to understand the transverse distribution of the accelerated electrons, the X-rays or the RF waves. For this, the beam block (see Section 3.3) was moved inside the beampipe ($z_b = 20$ cm from the gas jet) and the charges on the FC were measured at different block positions y_b . The origin $y_b = 0$ mm is chosen to be the beam block position where half of the beampipe (radius $r_{bp} = 6$ cm) is covered. With this measurement the transverse profile of the accelerated electron bunches can be estimated. The projected electron flux can be extracted by taking the derivative of the charge measured on the FC with respect to the blade's position. This means that the flux is highest where the charge changes most as a function of the beam block position y_b .

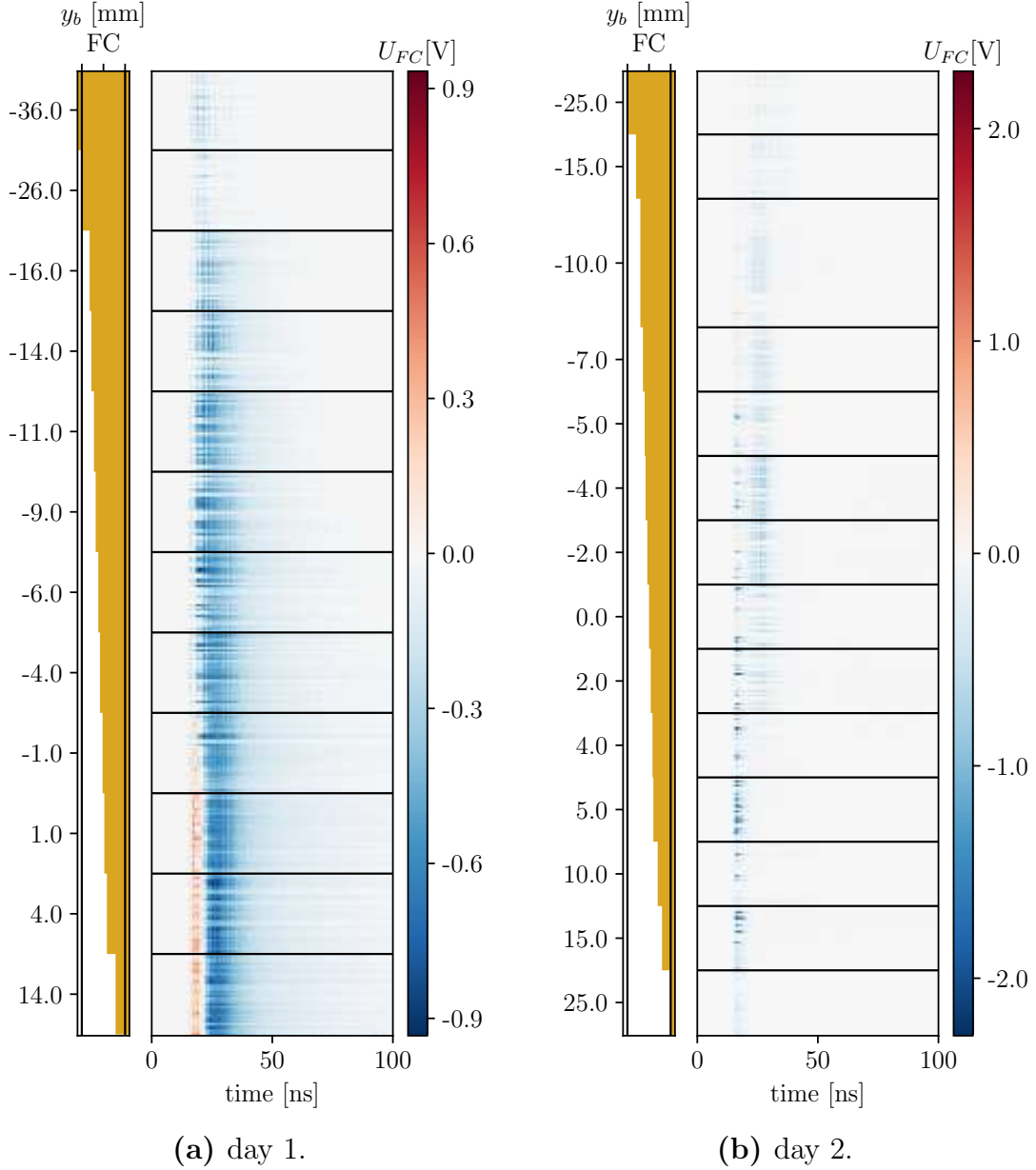


Figure 32: Signal on the FC as function of beam block position in the vacuum chamber. The colors correspond to the voltage U_{FC} in volts. At $y_b = 0$ mm the edge of the copper block was in the center of the vacuum chamber. All signals that are within two black horizontal lines are measured at the same y_b .

Day 1 In Figure 32, a stack of all the signals measured at the different beam block positions is shown. The positive feature of the signal at day 1 (see Figure 29a) disappeared within a small distance of a few mm when the edge of the beam block was close to the center of the beampipe $y_b = 0$ mm. This can also be seen in Figure 33c where the positive peak voltage is plotted against the block position y_b . This means that whatever was causing the positive peak was traveling along the laser axis and was confined to a few mm.

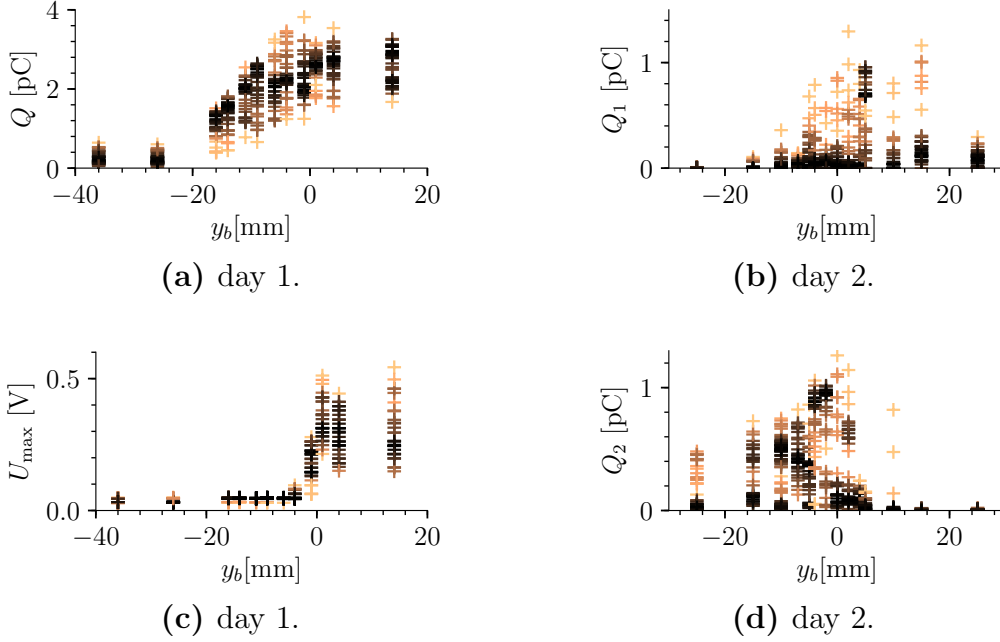


Figure 33: Charge on the FC for different beam block positions on day 1 and day 2. Q is the charge integrated from 0 ns to 100 ns. Q_1 (13 ns to 19 ns) and Q_2 (19 ns to 100 ns) are the charges contained in the peak and the wiggles (see Figure 29d). U_{max} is the height of the positive peak on day 1.

The total charge Q deposited on the FC decreased slowly with the block position y_b (see Figure 33a). The hole in the aluminum shielding of the FC was on the left side ($y < 0$) of the FC. This might explain why the biggest changes in charge were observed at the positions of $y_b < 0$.

Day 2 Especially interesting are the signals measured on day 2, because they were probably related to electrons accelerated to high energies ($E_{kin} > 32$ keV). When the block was inserted into the beam, an additional feature appeared in the signal of the FC (see Figure 29d). To separate the contributions of the two different features to the total charge measured on the FC, the charge integral was split in two, Q_1 (13 ns to 19 ns) and Q_2 (19 ns to 100 ns). When the beam block was not inserted ($y_b = 25$ mm) $Q_2 = 0$ pC and $Q_1 > 0$ pC (see Figure 29c). Thus, Q_1 is the charge of the accelerated electron bunch. Figure 33b suggests that electron beams with charges up to 1 pC were co-propagating with the laser. They had a size of about one centimeter at the beam block. Therefore, the divergence was roughly 20 mrad.

Q_2 abruptly increased when $y_b \approx 0$ mm and then slowly decreased as the block was inserted further into the beampipe (see Figure 33d). This suggests that the second feature in the signal came from low energetic secondary electrons or X-rays generated at the edge of the beam block.

In order to verify that the first peak on day 2 indeed came from electrons flying through

the beampipe, the beam size measurement was repeated with a permanent magnet fixed close to the beampipe. Figure 34 shows that the first peak of the signal was strongly

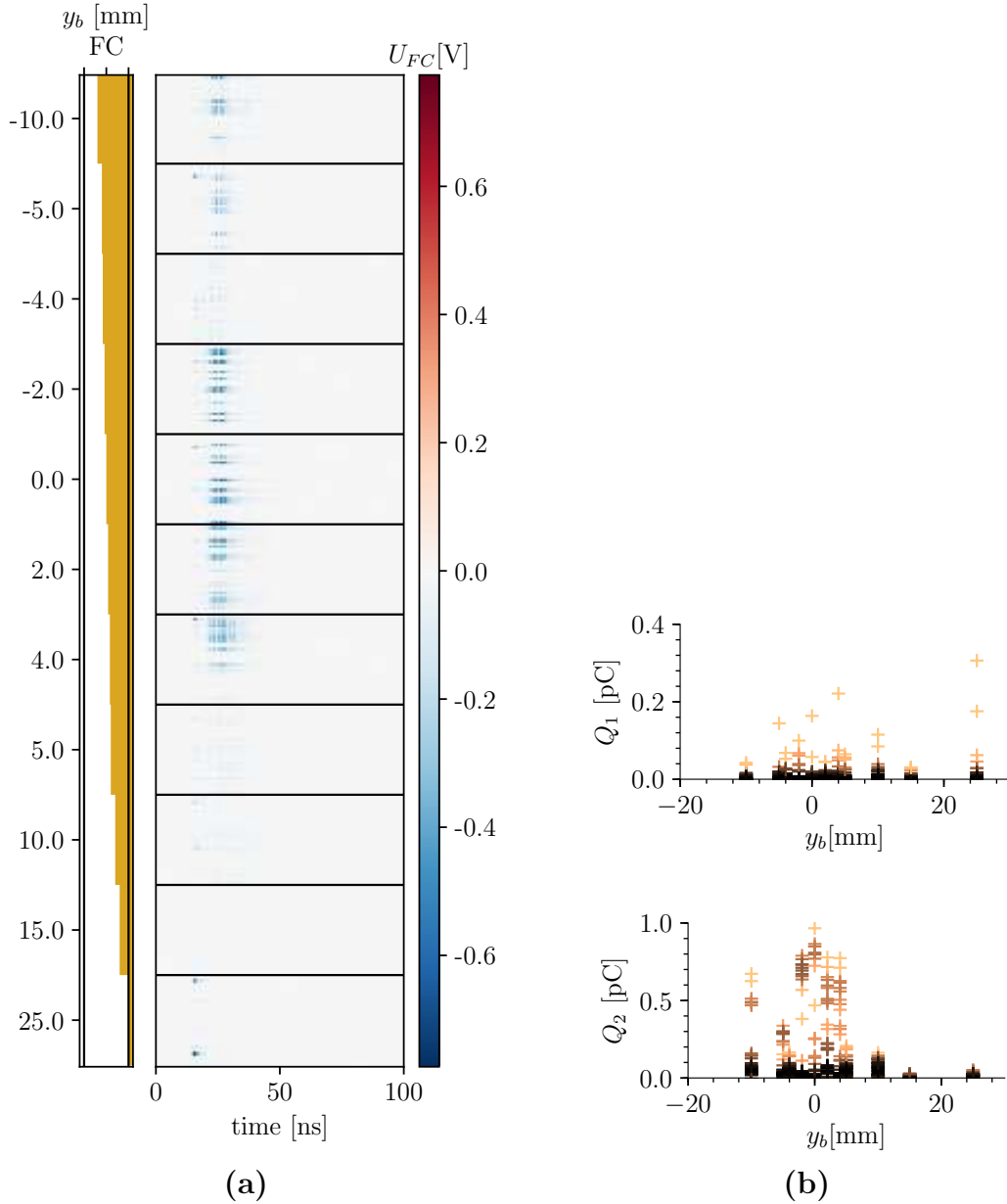


Figure 34: Signal on the FC as function of beam bock position y_b for day 2 with a magnet held close to the beampipe. Q_1 (13 ns to 19 ns) and Q_2 (19 ns to 100 ns) are the charges contained in the peak and in the wiggles.

affected by the magnet. The maximal charge on the FC decreased by a factor 4 when the magnet was introduced. However, the majority of shots had charges that were more than a factor 20 smaller. Because only very few shots had high charges, the energy distribution could not be estimated. The magnetic field was such that electrons with kinetic energies below (56 ± 7) keV could not reach the FC anymore. This cut-off energy is of similar order as the blocking energy of the aluminum foil (32 keV) and would explain the

large fluctuations of the signal. Only a few electron bunches with energies of the order of 60 keV were observed. The majority of them had energies of the order of the cut-off at 32 keV (see Figure 33b).

6 Outlook

The results of the experiments conducted during this thesis suggest that electrons have been accelerated. The charges and divergences of the electron bunches were measured (see Section 5). The low energies of the order of 60 keV can be explained by the laser parameters (see Table 1). To further increase charge and energy, more time has to be invested to understand limitations and to optimize the focal spot size, the pulse length and the energy of the laser pulse. After verifying the results presented in Section 5, the following measurements and changes to the experimental setup could be made:

Installation of Additional Diagnostics

- Laser:
 - Wavefront sensor
 - Calibrated photo diode for shot-to-shot energy measurement at IP
 - Additional pulse length measurement device, complementary to WIZZLER
- Gas Jet:
 - Fast digital pressure sensor right before nozzle
- Electron Diagnostics:
 - Pickup (PU) for detection of beam wakefield
 - Integrated Current Transformer as complementary measurement to FC
 - More sensitive scintillating screen like BIOMAX [7]

Before further experiments are conducted, additional diagnostics tools to measure more parameters of the laser, the gas jet and the electrons should be installed. A laser wavefront sensor directly before the parabolic mirror would make it possible to measure whether the large focal spot size is caused by a distorted wavefront. In the long term, a deformable mirror should be installed to correct for unwanted distortions. Additionally, the signal on the photo diode should be calibrated with the energy of the laser at the interaction point, so that real-time shot-to-shot measurements of the pulse energies are possible. To test the results of the WIZZLER, other pulse length measurements should be setup. For a better control on the configuration of the gas jet, a fast digital pressure sensor should be installed right before the nozzle. So far the pressure is read visually from an analog gauge. Finally, the electron diagnostics should be extended. In addition to the FC, a pickup for the detection of the beam's wakefield should be installed. If the signal on the pickup agrees with the signal on the FC, the signals on the FC are generated by RF. This prevents signals generated through leaks in the shielding of the FC to be interpreted as accelerated charge. An integrated current transformer could give complementary results to the charge measured by the FC.

Suggested Near Future Experiments A big leap for the experiment would be to detect the beam on a scintillating screen. This would allow for shot-to-shot divergence measurements and optimizations. In order to detect electrons on a scintillator, the charge and energy of the electrons need to be optimized. To do so, the cut-off energy of the FC should be raised by using more layers of aluminum foil. After optimizing the charge on the FC (not necessarily very stable) the screen can be inserted. If the light intensity generated by electrons hitting the screen is not high enough to be detected with the camera, the beam should first be focused by inserting the tunable permanent magnet triplet. After a signal is detected on the screen, I suggest setting up the entire spectrometer and studying the dependence of the energy distribution on the accelerator's configuration.

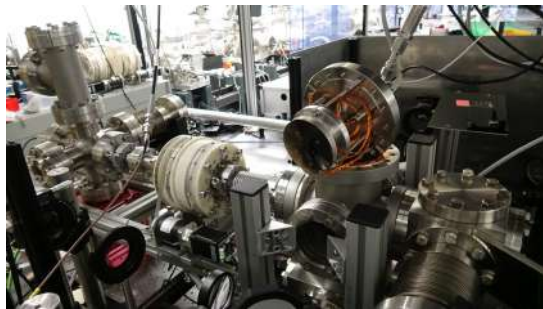
Applications of the Experiment The experiment could be used for educational purposes because it combines important concepts from both laser and accelerator physics. It would be interesting for students to learn about them in a hands-on internship, like it is the case in the advanced physics laboratory courses during the ETH Zurich undergraduate physics studies.

An interesting experiment would be to focus the beam down to a few tens of μm and inject it into a dielectric acceleration structure, which can be pumped by an intense Terahertz pulse, generated by one of the two other beamlines in the laser laboratory. This would allow to study the properties of accelerators based on dielectric structures without requiring beamtime at the SwissFEL.

If the laser parameters could be improved such that electrons ($\sim 1\text{ pC}$) are injected and accelerated to high energies ($\sim 5\text{ MeV}$) with a repetition rate of 100 Hz , the experiment would be interesting for transmission electron microscopy (TEM). The short electron bunches ($< 100\text{ fs}$) would allow imaging of ultrafast processes in materials with significant statistics [28].

7 Appendix

7.1 Image Collection



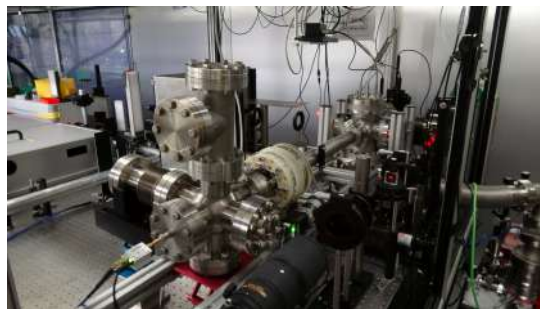
(a)



(b)



(c)



(d)



(e)

Figure 35: *Images of the experimental setup in the Aramis laser laboratory. Image (a) shows the accelerator with the permanent magnet dipole around the beampipe. The beam diagnostics unit with the movable block and the Faraday cup is on the left. The laser comes from the right. Image (b) shows the gas jet with blade after several shots with the laser. Image (c) is an image of the laser. The green light comes from the pump lasers. In image (d) on can see the illumination of the setup when the plasma is created.*

7.2 Multipole Moments of Permanent Magnets

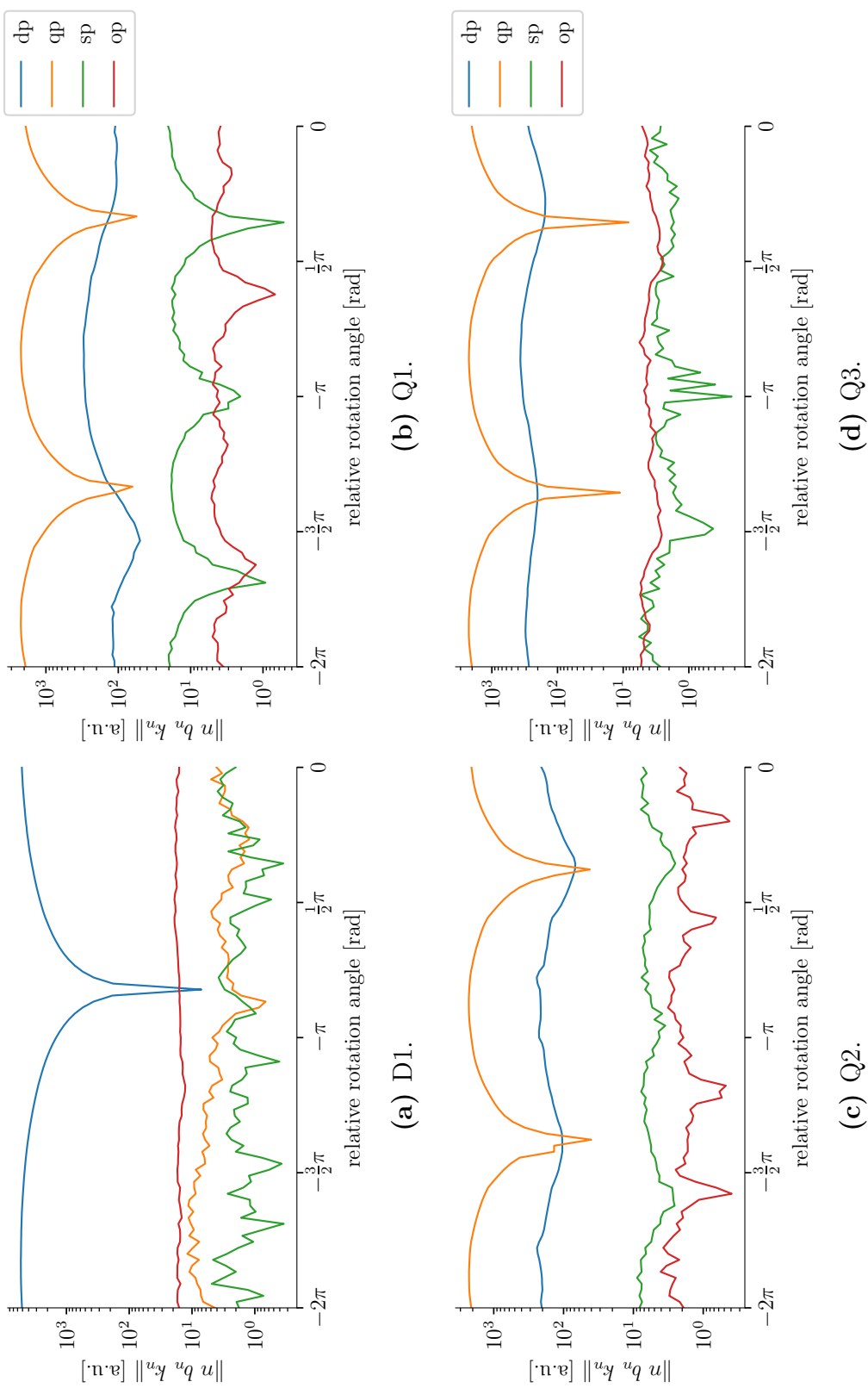


Figure 36: Dependence of multipole moments on relative rotation of Habach rings.

7.3 Field Maps of Permanent Magnet Lattice Elements

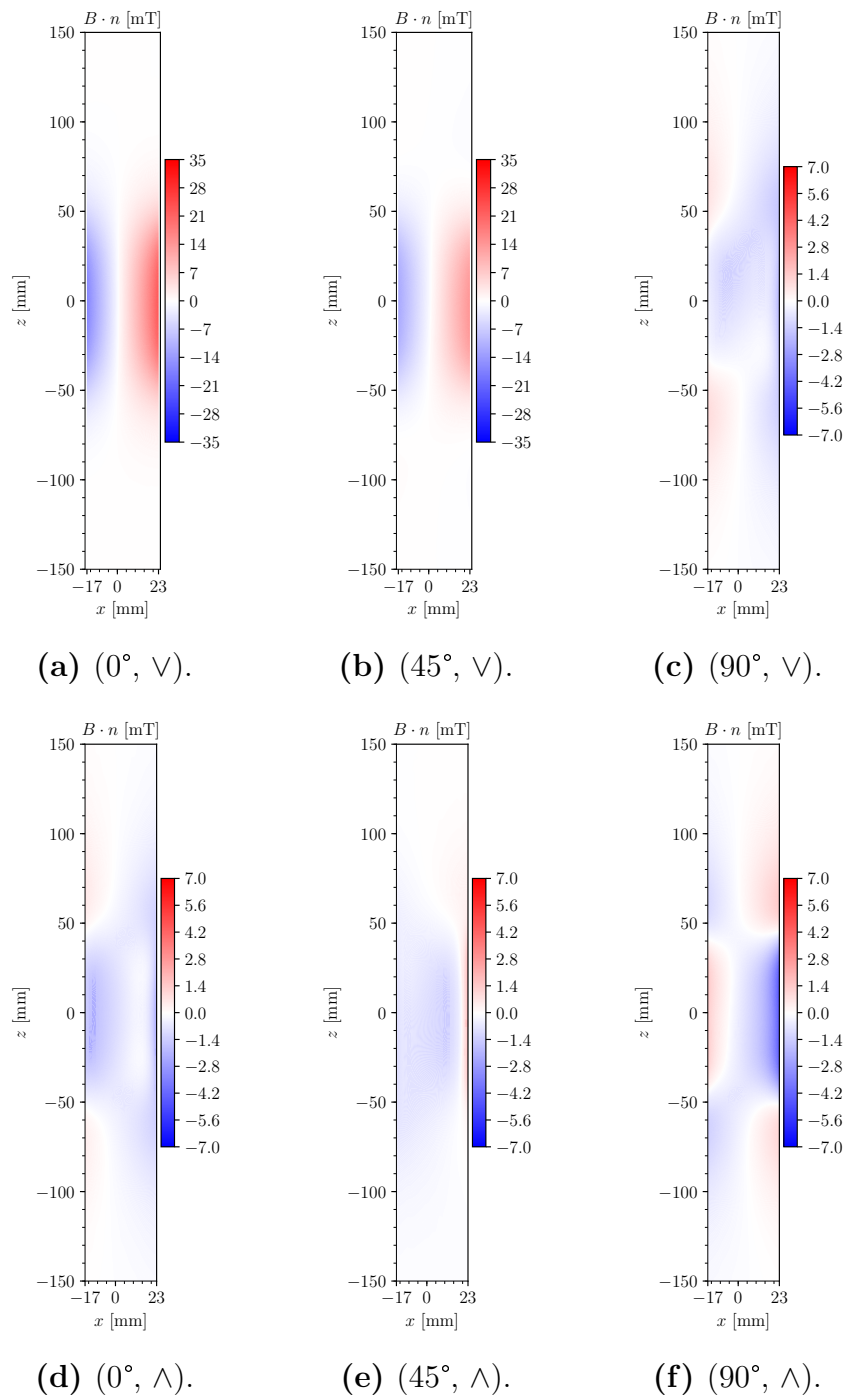


Figure 37: Field maps of the Q1 magnet in the configurations: a: gradient maximal and $b_2 \propto i$, b: gradient maximal and $b_2 \propto 1 + i$, c: gradient maximal and $b_2 \propto 1$, d: gradient minimal and $b_2 \propto i$, e: gradient minimal and $b_2 \propto 1 + i$, f: gradient minimal and $b_2 \propto 1$.

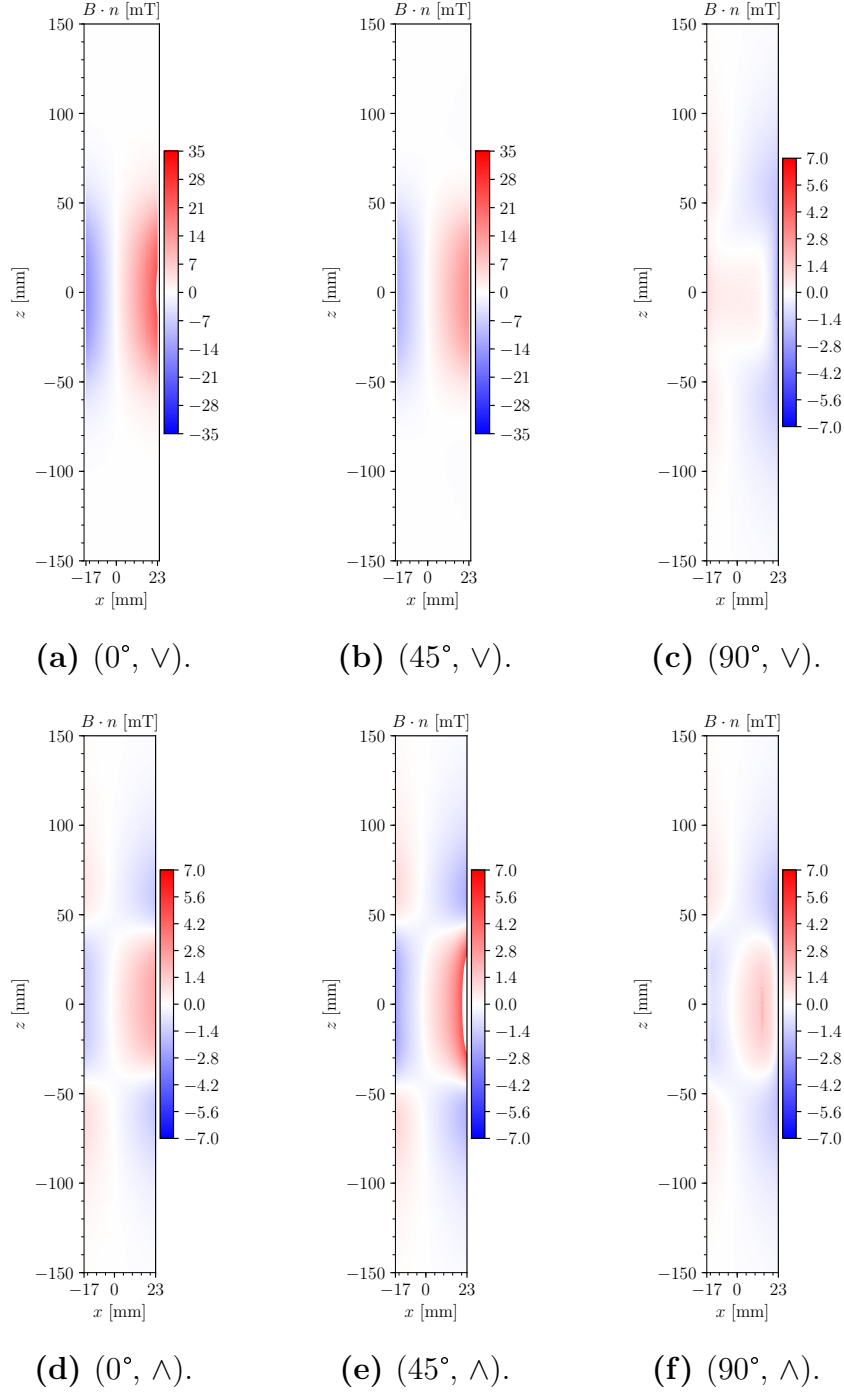


Figure 38: Field maps of the Q2 magnet in the configurations: a: gradient maximal and $b_2 \propto i$, b: gradient maximal and $b_2 \propto 1 + i$, c: gradient maximal and $b_2 \propto 1$, d: gradient minimal and $b_2 \propto i$, e: gradient minimal and $b_2 \propto 1 + i$, f: gradient minimal and $b_2 \propto 1$.

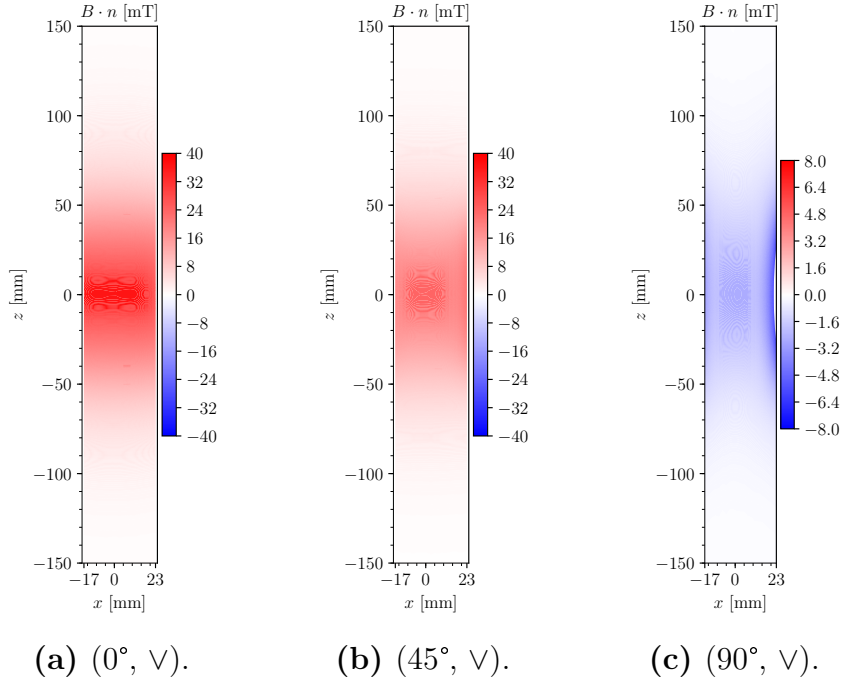


Figure 39: Field maps of the D1 magnet in the configurations: *a*: gradient maximal and $b_1 \propto i$, *b*: gradient maximal and $b_1 \propto 1 + i$, *c*: gradient maximal and $b_1 \propto 1$.

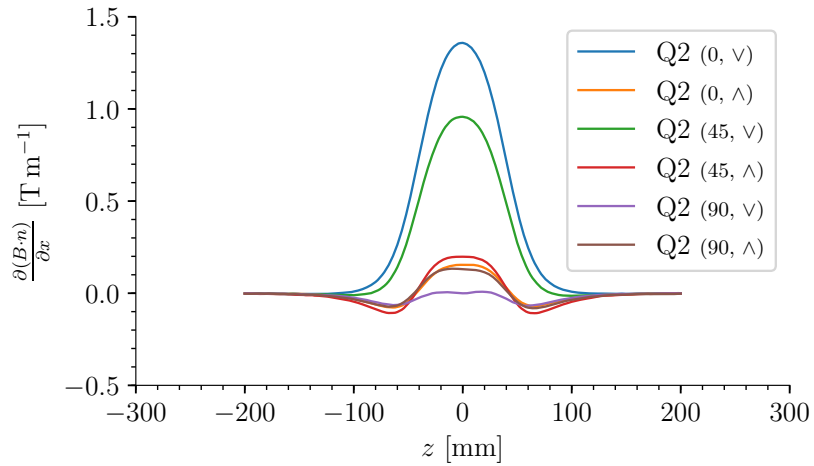


Figure 40: Gradient of quadrupole magnet Q2.

7.4 Collection of Python Scripts

7.4.1 Residue Calculation

```
import sympy as sym

u = sym.Symbol('u')

def fac(n):
    res = 1
    for i in range(n):
        res *= i+1
    return res

def res(a, f, order, display = False):
    g = (u - a)**order * f/ fac(order - 1)
    g = sym.simplify(g)
    if display:
        print(g)
    for i in range(order - 1):
        g = sym.simplify(sym.diff(g, u))
    if display:
        print(g)
    return sym.simplify(g.subs(u, a))
```

7.4.2 Focus Optimization

```
def optimize(self, sleep_time = 0.2, output = True):
    #this variable is necessary to compensate the attenuation of the laser
    global intmult
    intmult = 1.

    wanted_focus_um = self.focus_min

    maxiter = self.maxiter
    n_av = self.n_av

    global reduce_int
    reduce_int = False
    def to_min():
        global intmult

        FWHMxs = []
        FWHMys = []
        maxints = []
        for i in range(n_av):
            measurement = self.focus.measure()
            FWHMxs.append(measurement['FWHMx'])
            FWHMys.append(measurement['FWHMMy'])
            maxints.append(measurement['maxit'])

        if output:
            self.focus.plot_measure(measurement)
```

```

del measurement

if output:
    print ('FWHMxs: ',FWHMxs)
    print ('FWHMys: ',FWHMys)
    print ('maxints: ',maxints)
    print ('mean(maxints): ',np.mean(maxints))

res = np.sqrt((np.array(FWHMxs)**2 + np.array(FWHMys)**2)/2 + (np.
                array(FWHMxs) - np.array(
                FWHMys)) **2)
mean, error = np.mean(res), np.std(res, ddof = -1)/np.sqrt(len(res)
)

global reduce_int
if np.mean(maxints) > 4e3:
    reduce_int = True
    print ('will be attenuated')

if output:
    print ('mean: ',mean,'error: ', error)

if mean < wanted_focus_um:
    if output:
        print ('The optimization converged. Final value: ',mean)
    return

return mean, error

```

7.4.3 Example Device (test_device1.py)

```

import numpy as np
import matplotlib.pyplot as plt

from Scripts.PlottingServers import Plot1DServer

'''
config file:

idl:                int
okasdasd:           boolean

measurement file:

value:              list of rands (length is idl)
random:             float64 random number
'''

default_config = {'idl': 5,
                  'okasdasd': True}

class test_device1:
    def __init__(self, config):

```

```

self.config = config

self.plot_server = None

@property
def config(self):
    config = {}
    config['idl'] = self.id
    config['okasdasd'] = self.ok
    return config

@config.setter
def config(self, config):
    self.id = config['idl']
    self.ok = config['okasdasd']

def measure(self):
    measurement = {}
    measurement['value'] = np.random.rand(int(np.round(self.id,0)))
    measurement['random'] = np.random.rand()
    return measurement

def plot_measure(self, measurement, config = None):
    if self.plot_server == None:
        self.plot_server = Plot1DServer({'title':'test_device1', '
                                         xlabel':'num', 'ylabel':
                                         'rand'})

    self.plot_server.update(range(len(measurement['value'])),
                             measurement['value'])

def spec_home(self):
    print ('this stuff will be homed')

```

References

- [1] A. Adelman et al. “Realtime Tomography of Gas-Jets with a Wollaston Interferometer”. In: (Nov. 2017). arXiv: 1711.02480. URL: <http://arxiv.org/abs/1711.02480>.
- [2] P. Arpaia et al. “Rotating-coil calibration in a reference quadrupole, considering roll-angle misalignment and higher-order harmonics”. In: *Measurement* 87 (June 2016), pp. 74–82. ISSN: 0263-2241. DOI: 10.1016/J.MEASUREMENT.2016.02.061. URL: <https://www.sciencedirect.com/science/article/pii/S0263224116001482>.
- [3] Pasquale Arpaia et al. “A polyvalent harmonic coil testing method for small-aperture magnets”. In: *Review of Scientific Instruments* 83.8 (Aug. 2012), p. 085116. ISSN: 0034-6748. DOI: 10.1063/1.4746281. URL: <http://aip.scitation.org/doi/10.1063/1.4746281>.
- [4] S. K. Barber et al. “Measured Emittance Dependence on the Injection Method in Laser Plasma Accelerators”. In: *Physical Review Letters* 119.10 (Sept. 2017), p. 104801. ISSN: 0031-9007. DOI: 10.1103/PhysRevLett.119.104801. URL: <https://link.aps.org/doi/10.1103/PhysRevLett.119.104801>.
- [5] *Become a Master of Backside Wakesurfing - LIFEFORM LED*. URL: <http://lifeformled.com/blog/become-a-master-of-backside-wakesurfing/> (visited on 12/07/2017).
- [6] Peter Blümler. “Proposal for a permanent magnet system with a constant gradient mechanically adjustable in direction and strength”. In: *Concepts in Magnetic Resonance Part B: Magnetic Resonance Engineering* 46.1 (2016), pp. 41–48. ISSN: 1552504X. DOI: 10.1002/cmr.b.21320. URL: <https://arxiv.org/pdf/1510.02772.pdf>.
- [7] Alexander Buck. “Advanced characterization and control of laser wakefield acceleration”. PhD thesis. Sept. 2011, p. 144. URL: <https://edoc.ub.uni-muenchen.de/13461/>.
- [8] Henrik Ekerfelt, Olle Lundh, and Martin Hansson. “Parametric study of density down-ramp injection in laser wakefield acceleration”. In: (2014). URL: <http://lup.lub.lu.se/luur/download?func=downloadFile%7B%5C%7DrecordOID=5368172%7B%5C%7DfileOID=7357104>.
- [9] E Esarey, C B Schroeder, and W P Leemans. “Physics of laser-driven plasma-based electron accelerators”. In: *Reviews of Modern Physics* 81.3 (2009), pp. 1229–1285. ISSN: 00346861. DOI: 10.1103/RevModPhys.81.1229. URL: <http://bella.lbl.gov/wp-content/uploads/sites/42/2015/08/RevModPhys.81.1229.pdf>.

- [10] K. Halbach. “Design of permanent multipole magnets with oriented rare earth cobalt material”. In: *Nuclear Instruments and Methods* 169.1 (Feb. 1980), pp. 1–10. ISSN: 0029554X. DOI: 10.1016/0029-554X(80)90094-4. URL: <http://linkinghub.elsevier.com/retrieve/pii/0029554X80900944>.
- [11] Z. H. He et al. “High repetition-rate wakefield electron source generated by few-millijoule, 30 fs laser pulses on a density downramp”. In: *New Journal of Physics* 15.5 (May 2013), p. 053016. ISSN: 13672630. DOI: 10.1088/1367-2630/15/5/053016. arXiv: arXiv:1204.6414v1. URL: <http://stacks.iop.org/1367-2630/15/i=5/a=053016?key=crossref.fd509d203751130879517419ba4a28cd>.
- [12] B. Hermann. *Schlieren Interferometry of a Pulsed Gas Jet*. ETH Zurich, Paul-Scherrer-Institut. 2016. URL: http://amas.web.psi.ch/people/aadelmann/ETH-Accel-Lecture-1/projectscompleted/phys/Semester_Thesis-BH.pdf.
- [13] B. Hermann. *Single Beam Wollaston Interferometry of a Gas Jet with non-Uniform Density towards Laser Wakefield Acceleration*. ETH Zurich, Paul Scherrer Institut. 2017. URL: <http://amas.web.psi.ch/people/aadelmann/ETH-Accel-Lecture-1/projectscompleted/phys/hermann.pdf>.
- [14] D. Kaplan and P. Tournois. “Theory and performance of the acousto optic programmable dispersive filter used for femtosecond laser pulse shaping”. In: *Journal de Physique IV (Proceedings)* 12.5 (June 2002), pp. 69–75. ISSN: 1155-4339. DOI: 10.1051/jp4:20020098. URL: <http://www.edpsciences.org/10.1051/jp4:20020098>.
- [15] Thomas Kluyver et al. “Jupyter Notebooks, a publishing format for reproducible computational workflows”. 2016. URL: <https://eprints.soton.ac.uk/403913/>.
- [16] Ardana Lamas. “Femtosecond electron and X-ray source developments for time-resolved applications”. In: 6938 (2016). DOI: 10.5075/EPFL-THESIS-6938. URL: <https://infoscience.epfl.ch/record/218627>.
- [17] Rémi Lehe. “Improvement of laser-wakefield accelerators: towards a compact free electron laser”. Theses. Ecole Polytechnique, July 2014. URL: <https://pastel.archives-ouvertes.fr/tel-01088398>.
- [18] Steven M. Lund and Klaus Halbach. “Iron-free permanent magnet systems for charged particle beam optics”. In: *Fusion Engineering and Design* 32-33.1-4 (Nov. 1996), pp. 401–415. ISSN: 09203796. DOI: 10.1016/S0920-3796(96)00496-6. URL: <http://linkinghub.elsevier.com/retrieve/pii/S0920379696004966>.

- [19] Arnold Magnetics. *RECOMA $\frac{1}{2}$ 35E - The World's Most Power Dense Samarium Cobalt Magnet Material*. [Online; accessed 4-December-2017]. 2017. URL: <http://www.arnoldmagnetics.com/en-us/Products/RECOMA-Samarium-Cobalt/RECOMA-35E>.
- [20] A. Moulet et al. "Single-shot, high-dynamic-range measurement of sub-15 fs pulses by self-referenced spectral interferometry". In: *Optics Letters* 35.22 (Nov. 2010), p. 3856. ISSN: 0146-9592. DOI: 10.1364/OL.35.003856. URL: <https://www.osapublishing.org/abstract.cfm?URI=ol-35-22-3856>.
- [21] L P Ovsyannikova and T Ya Fishkova. "Electromagnetic quadrupole-octupole lens". In: *Pis'ma Zh. Tekh. Fiz* 25 (1999), pp. 5–7. URL: <https://link.springer.com/content/pdf/10.1134/1.1262657.pdf>.
- [22] F. Pedregosa et al. "Scikit-learn: Machine Learning in Python". In: *Journal of Machine Learning Research* 12 (2011), pp. 2825–2830.
- [23] Stefan Ritt. *ELOG User's Guide*. <https://midas.psi.ch/elog/userguide.html>. Accessed: 2017-12-03. 2017.
- [24] N. Sauerwein. *Design study for Laser Plasma Wakefield Acceleration of low Energy Electrons*. ETH Zurich, Paul Scherrer Institut. 2016. URL: <http://amas.web.psi.ch/people/aadelmann/ETH-Accel-Lecture-1/projectscompleted/phys/Wake.pdf>.
- [25] N. Sauerwein. *Theory and Experimental Test of Electron Spectrometers for Laser Wakefield Accelerators*. Ecole Polytechnique Paris, LLR, CNRS, CEA. 2017. URL: <http://amas.web.psi.ch/people/aadelmann/ETH-Accel-Lecture-1/projectscompleted/phys/nickparis.pdf>.
- [26] K Schmid et al. "Density-transition based electron injector for laser driven wakefield accelerators". In: *Physical Review Special Topics - Accelerators and Beams* 13.9 (2010). ISSN: 10984402. DOI: 10.1103/PhysRevSTAB.13.091301. URL: <https://journals.aps.org/prab/pdf/10.1103/PhysRevSTAB.13.091301>.
- [27] P. Sprangle et al. "Propagation and guiding of intense laser pulses in plasmas". In: *Physical Review Letters* 69.15 (Oct. 1992), pp. 2200–2203. ISSN: 0031-9007. DOI: 10.1103/PhysRevLett.69.2200. URL: <https://link.aps.org/doi/10.1103/PhysRevLett.69.2200>.
- [28] Ramesh Srinivasan et al. "Ultrafast Electron Diffraction (UED)". In: *Helvetica Chimica Acta* 86.6 (June 2003), pp. 1761–1799. ISSN: 0018019X. DOI: 10.1002/hlca.200390147. URL: <http://doi.wiley.com/10.1002/hlca.200390147> <http://onlinelibrary.wiley.com/doi/10.1002/hlca.200390147/full%7B%5C%7D5Cnhttp://doi.wiley.com/10.1002/hlca.200390147>.

- [29] K Swanson et al. “Electron beam control using shock-induced density downramp injection”. In: *AIP Conference Proceedings* 1812.040004 (2017). DOI: 10.1063/1.4975851. URL: <http://dx.doi.org/10.1063/1.4975851>
<http://aip.scitation.org/toc/apc/1812/1>.
- [30] Warp team. *Warp*. [Online; accessed 4-December-2017]. 2017. URL: <http://warp.lbl.gov/>.
- [31] A. Trisorio et al. “Self-referenced spectral interferometry for ultrashort infrared pulse characterization”. In: *Optics Letters* 37.14 (July 2012), p. 2892. ISSN: 0146-9592. DOI: 10.1364/OL.37.002892. URL: <https://www.osapublishing.org/abstract.cfm?URI=ol-37-14-2892>.
- [32] Stéfan van der Walt et al. “scikit-image: image processing in Python”. In: *PeerJ* 2 (June 2014), e453. ISSN: 2167-8359. DOI: 10.7717/peerj.453. URL: <http://dx.doi.org/10.7717/peerj.453>.
- [33] R. Weingartner et al. “Ultralow emittance electron beams from a laser-wakefield accelerator”. In: *Physical Review Special Topics - Accelerators and Beams* 15.11 (Nov. 2012), p. 111302. ISSN: 1098-4402. DOI: 10.1103/PhysRevSTAB.15.111302. URL: <https://link.aps.org/doi/10.1103/PhysRevSTAB.15.111302>.
- [34] Wikipedia. *Nelder-Mead method* — *Wikipedia, The Free Encyclopedia*. [Online; accessed 4-December-2017]. 2017. URL: https://en.wikipedia.org/w/index.php?title=Nelder%E2%80%93Mead_method&oldid=811113017.
- [35] Wikipedia. *Wakesurfing* — *Wikipedia, The Free Encyclopedia*. [Online; accessed 4-December-2017]. 2017. URL: <https://en.wikipedia.org/w/index.php?title=Wakesurfing&oldid=808239941>.